



# Electro-osmotic oscillatory flow of viscoelastic fluids in a microchannel

Samir H. Sadek, Fernando T. Pinho\*

CEFT, Departamento de Engenharia Mecânica, Faculdade de Engenharia da Universidade do Porto, Rua Dr. Roberto Frias, 4200-465 Porto, Portugal

## ARTICLE INFO

### Keywords:

Microchannels  
Electro-osmotic flow (EOF)  
Viscoelastic fluids  
Small amplitude oscillatory shear flow (SAOS)  
Small amplitude oscillatory shear by electro-osmosis (SAOSEO)  
Multi-mode upper-convected Maxwell (UCM) model

## ABSTRACT

This work presents an analytical solution for electro-osmotic flow (EOF) in small amplitude oscillatory shear (SAOS) as a measuring tool suitable to characterize the linear viscoelastic properties of non-Newtonian fluids in microchannel flow. The flow in the straight microchannel is driven by applying oscillating sinusoidal electric potentials. Fourier series are used to derive an expression for the velocity field, under an externally imposed generic potential field aimed at the practical application of SAOS in characterizing the rheological properties of viscoelastic fluids. This extensive investigation covers a wide range of parameters and considers the multi-mode upper-convected Maxwell (UCM) model, which represents the rheology of viscoelastic fluids in the limit of small and slow deformations. Particular focus is given to two cases of practical interest: equal wall zeta potentials at both channel walls and negligible zeta potential at one of the walls. The results show that in flows with thin electric double layers (EDL), Reynolds numbers below 0.001, and Deborah numbers below 100, corresponding to a viscoelastic Mach number of 0.32, the velocity field outside the EDLs is linear and has a large enough amplitude of oscillation, which may allow the quantification of the storage and loss moduli in the linear regime. This technique requires the use of significantly smaller sample sizes than the traditional SAOS in a rotational rheometer.

## List of abbreviations

EDL	electric double layer
EOF	electro-osmotic flow
EZP	equal zeta potential
NZP	negligible zeta potential
PIV	particle image velocimetry
PTV	particle tracking velocimetry
SAOS	small amplitude oscillatory shear
SAOSEO	small amplitude oscillatory shear by electro-osmosis

## 1. Introduction

Transport phenomena at the micro-scale is increasingly of interest for applications in a variety of systems given the inherent savings in materials and energy, fast reaction times and the ability of today's technology to fabricate micro-systems with multi-purpose functions. In particular, micro-scale systems are increasingly being used to process bio-fluids and chemicals, in species separation, or mixing, among others. On moving from macro to micro-scale systems, the ratio of volume to surface forces dramatically decreases and surface-based forcing mechanisms become advantageous relative to volume-based methods. Indeed, monitoring and controlling liquid transport accurately by electro-osmosis becomes increasingly easier and more effective at the micro- and nano-scales, whereas the use of the traditional pressure gradient driven flow becomes

increasingly less efficient as the size of the channels are reduced due to the significant increase of the pressure gradients [1–3].

Electro-osmosis is an electro-kinetic phenomenon, identified first by Reuss [4] in the 19th century. In electro-osmosis, chemical equilibrium between a polar fluid and a solid dielectric wall results on a spontaneous charge being acquired by the wall and the corresponding counter-charge occurring in near-wall layers on the liquid side. On the liquid side, a very thin wall layer of immobile counter-ions develops and is followed by a thicker layer of diffuse counter-ions, thus creating the so-called electric double layer (EDL). Upon application of an external electric potential field between the inlet and outlet of the microchannel the ensuing motion of the diffuse layer counter-ions drags the remaining core fluid in the channel by viscous forces. An overview of electro-osmosis and of other electro-kinetic flow techniques can be found in [5–7]. Electro-osmosis offers special unique features over other types of pumping methods (e.g. micro-pumps), and has the ability of easily and very quickly (within the viscous time scale) change flow direction and magnitude by changing the applied potential field. The generated flow is defined by the pattern of the imposed electric potential field, so it can be easily driven at constant flow rate, or following an oscillatory pattern [8].

As previously mentioned, chemical and biomedical lab-on-a-chip systems are the most frequent applications of micro-scale liquid flows. The fluids are frequently made from complex molecules which exhibit non-linear rheological behavior. These so-called non-Newtonian fluids have such rheological characteristics as variable viscosity and viscoelasticity. The rheological characterization of non-Newtonian fluids is performed with various controllable and quasi-controllable flows

\* Corresponding author.

E-mail address: [fpinho@fe.up.pt](mailto:fpinho@fe.up.pt) (F.T. Pinho).

(i.e., flows with known kinematics) which is independent or weakly dependent on the fluid properties to be measured [9]. One such flow is the small amplitude oscillatory shear (SAOS) flow used to characterize the linear viscoelastic behavior of complex fluids. This Couette-type flow is usually implemented in rotational rheometers, but linear viscoelasticity can also be assessed via other oscillatory flows provided the amplitude of the oscillations are small and slow enough to make the fluid response independent of the amount of deformation and only dependent on the oscillating frequency and fluid material functions.

Oscillatory channel flow can be driven by an imposed harmonic motion of the sidewalls or an oscillating pressure gradient in the streamwise direction. Even though these are qualitatively similar, from a mathematical point of view they are slightly different: whereas the first approach imposes strain and monitors stress, the second one imposes the stress and monitors the strain. In this work, we explore the use of the oscillatory electro-osmotic flow (EOF) as a method to characterize the linear viscoelasticity of non-Newtonian fluids. This is achieved through a general solution by adopting the multi-mode upper-convected Maxwell (UCM) model. It is well known that in the limit of small and slow deformations the response of complex viscoelastic constitutive models reduces to that of the UCM model [10], which in turn behaves as a linear viscoelastic model in such limit. In turn, multi-mode models allow a better description of real fluids, which possess spectra of relaxation times rather than single characteristic time scales [11]. The concept has been around for more than a century in the form of the generalized Maxwell model (also called the Maxwell-Wiechert model) for linear viscoelasticity.

The multi-mode UCM model has been used in a variety of practical computational and especially experimental applications. Thurston [12] used it to describe the complex rheology of blood, Renardy [13] relied on the multi-mode UCM model in his proof of existence of steady slow flows of viscoelastic fluids and, subsequently, Renardy [14] and Savelev and Renardy [15] addressed the conditions of flow controllability of viscoelastic fluids using again a multi-mode UCM fluid model. Computational applications were first addressed by Rajagopalan et al. [16], with the main convergence problem being always associated with the mode with the highest relaxation time. Of direct relevance to this work are the contributions addressing the computation of the storage and loss moduli for multi-mode models [11,17] in SAOS (i.e., for rotational rheometry). The use of the multi-mode UCM model to describe complex viscoelastic fluids and flows is also exemplified through the following diverse examples: predictions of the extrusion film casting process using a polymeric resin of two different macromolecular chains [18] and of polymer crystallization kinetics under non-isothermal flow conditions [19]; examining steady creeping flow behavior [16], large amplitude oscillatory shear (LAOS) flow [20] and characterization of complex viscoelastic properties of bovine liver tissue [21], and as well as brain tissue [22].

The remaining of this introduction addresses the contributions in EOF for non-Newtonian fluids in steady and especially unsteady flow. Starting with steady flows, Das and Chakraborty [23], and Chakraborty [24] were among the first to study analytically the momentum, heat and mass transfer in microchannel flows of non-Newtonian fluids driven by electrokinetic forces, but their work was limited to the power-law model. Other analytical investigations of steady electro-osmosis channel flows of power-law fluids were done by Zhao et al. [1], who invoked the Debye-Hückel approximation, and Zhao and Yang [25], who combined EO forcing with pressure-driven (PD) flow. These investigations are not necessarily a limitation, because the steady flow characteristics of viscoelastic fluids only depend on its viscosity law.

Park and Lee [26,27] were among the first to investigate numerically and analytically EOF with viscoelastic fluids. Of particular concern in [26] was the evaluation of the Helmholtz-Smoluchowski velocity in pure EOF by a simple cubic algebraic equation to be used as a wall function in the numerical calculations in order to bridge the electric double layer and avoid the use of very refined meshes near the walls. Park

and Lee [27] extended their previous numerical study to investigate the EOF of viscoelastic fluids, described by the Phan-Thien—Tanner (PTT) model, through a rectangular duct with and without a pressure gradient, including the prediction of its secondary flow. Afonso et al. [28] obtained the analytical solution for mixed electro-osmotic/pressure driven (EO/PD) channel flow for viscoelastic fluids described by the simplified PTT (sPTT) and the Finitely Extensible Non-linear Elastic (FENE-P) models. Still on steady EO channel flows of viscoelastic fluids, Afonso et al. [29] considered asymmetric wall zeta potentials for the sPTT and FENE-P models, whereas Dhinakaran et al. [30] analysed the critical shear rate and Deborah number for the onset of fluid instabilities of constitutive nature with the full PTT model.

As described previously, EOF motion starts once an external potential difference is applied across the electrodes embedded in a microchannel. The imposed driving potential may either correspond to a direct current EOF (DCEOF) or an alternating current EOF (ACEOF), with all previous steady flows concerning DCEOF. In ACEOF the flow depends on the amplitude and frequency of the applied electric field in addition to geometric, wall and fluid properties. Applying a non-uniform electric field leads to a nonzero time-average flow [31], whereas the use of a uniform field results in a zero time-average flow. This latter case is a special case of ACEOF, called time-periodic EOF, and the use of DCEOF is a limit case with zero frequency [5,32].

Dutta and Beskok [33] investigated analytically the two-dimensional flow of Newtonian fluids driven by time-periodic EOF in straight microchannels and presented the corresponding velocity field distribution for weak potential (no interaction between electric double layers (EDLs)). Subsequently, Chakraborty and Srivastava [34] studied analytically the flow through straight microchannels with overlapped EDLs.

Of more direct relevance to this work, Liu et al. [35] presented an analytical solution for one-dimensional electro-osmotic flow between oscillating micro-parallel plates of viscoelastic fluids represented by a single mode generalized Maxwell model. They considered a low zeta potential which allows the linearization of the Poisson-Boltzmann equation. Their equations for the dimensionless velocity profile and volumetric flow rate as a function of the oscillating Reynolds number, electrodynamic width, and normalized relaxation time, are useful to understand the flow characteristics of this flow configuration.

Oscillating flows of small amplitude are used in rotational rheology to probe the elastic nature of fluids in the linear regime. These are flow conditions that are also present in some electro-osmotic flows and the main motivation of this work is precisely the assessment of the feasibility and effectiveness of using oscillatory electro-osmotic shear flow in the rheological characterization of viscoelastic fluids. As previously explained, real fluids have a spectrum of time scales and here the fluid is precisely described by the multi-mode UCM model rather than by a single mode model as done in [35], thus to our best knowledge this problem has not yet been solved. In addition to providing the EOF solution for a multi-mode Maxwell fluid under the action of an oscillatory flow forcing, this work addresses the use of the flow as a novel measuring tool for small amplitude oscillatory shear flow driven by electro-osmosis (SAOSEO).

Section 2 starts with the continuity and momentum governing equations for the problem at hand along with the viscoelastic constitutive multi-mode UCM model being presented in Section 2.1. The distributions of the induced EDL potential field  $\psi$  and of the net electric-charge density  $\rho_e$ , with emphasis on two special cases corresponding to two different sets of wall boundary conditions, are presented in Section 2.2. Section 2.3 solves analytically the UCM constitutive equation and in Section 2.4 the flow problem at hand is solved using Fourier series for the more complex generic periodic signals of the imposed electric field. Section 3 discusses the analytical solution derived in the previous section and identifies the conditions that need to be satisfied for the obtained solution to be useful for rheometric purposes, which is detailed in Section 4. Finally, Section 5 concludes and summarizes the main findings of this work.

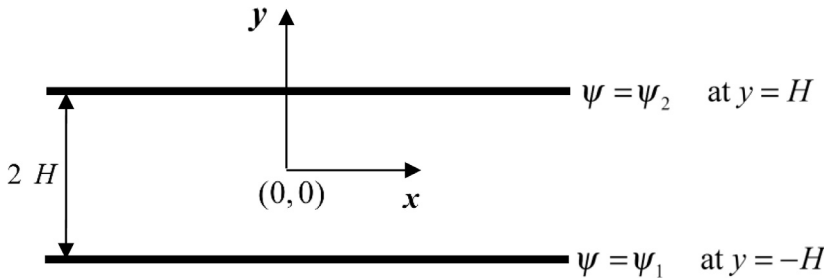


Fig. 1. Schematic diagram, illustrating the microchannel dimensions, coordinate system, and the induced potential boundary conditions.

2. Governing equations and analytical solution

The unsteady oscillatory shear flow of the incompressible viscoelastic fluid under investigation is sketched in Fig. 1, which shows the microchannel and the two-dimensional coordinate system used, with its origin located at the geometric symmetry plane. The channel height is 2H, the length is L, and the depth of the channel in the z direction is large, i.e., the flow field is assumed independent of the z coordinate. Fig. 1 also defines the boundary conditions at the upper and lower walls, where for the velocities there are no-slip boundary conditions, u(-H) = u(H) = 0, and for the induced electric potentials we consider the possibility of different zeta potentials at both walls, i.e., psi(-H) = psi\_1 and psi(H) = psi\_2.

The basic equations describing the flow under investigation are the continuity, and the Cauchy momentum equations:

$$\begin{aligned} \nabla \cdot \mathbf{u} &= 0, \\ \rho \frac{D\mathbf{u}}{Dt} &= -\nabla p + \nabla \cdot \boldsymbol{\tau} + \rho_e \mathbf{E} \end{aligned} \tag{1}$$

where rho is the fluid density (incompressible fluid assumption), t is the time, u is the velocity vector, p is the pressure, tau is the extra-stress tensor, rho\_e is the net electric-charge density associated with the spontaneous formation of electric double layers, and E is the applied external electric field. Assuming one-dimensional flow, the x-momentum equation simplifies to:

$$\rho \frac{\partial u}{\partial t} = \frac{\partial \tau_{xy}}{\partial y} + \rho_e E_x \tag{2}$$

We assume also that the flow is driven externally by an electric field, without any pressure gradients imposed, (nabla p = 0) and the flow is spatially fully-developed.

2.1. Constitutive equation

In this work we use the multi-mode UCM model, where the total extra-stress is expressed as the sum of m modes [36]:

$$\boldsymbol{\tau} = \sum_{n=1}^m \boldsymbol{\tau}_n \tag{3}$$

As explained in the introduction, the use of a multi-mode UCM model allows a more realistic description of fluid memory by a spectrum of relaxation times [11], including the contribution from a Newtonian solvent by considering a null relaxation time in one of the modes. For each mode, the extra-stress is expressed by the UCM model:

$$\boldsymbol{\tau} + \lambda \overset{\nabla}{\boldsymbol{\tau}} = 2\eta \mathbf{D} \tag{4}$$

where D = (nabla u^T + nabla u) / 2 is the deformation rate tensor, lambda is the relaxation time of the fluid, eta is the polymer viscosity coefficient (each mode has different lambda and eta), and nabla tau is the upper-convected derivative of tau, defined by:

$$\overset{\nabla}{\boldsymbol{\tau}} = \frac{D\boldsymbol{\tau}}{Dt} - \nabla \mathbf{u}^T \cdot \boldsymbol{\tau} - \boldsymbol{\tau} \cdot \nabla \mathbf{u} \tag{5}$$

Assuming that the flow instantaneously becomes fully-developed, a good approximation for low Reynolds number flows, Eq. (4) simplifies to:

$$\tau_{xx} + \lambda \frac{\partial \tau_{xx}}{\partial t} = 2\lambda \tau_{xy} \frac{\partial u}{\partial y} \tag{6}$$

$$\tau_{xy} + \lambda \frac{\partial \tau_{xy}}{\partial t} = \eta \frac{\partial u}{\partial y} \tag{7}$$

$$\tau_{yy} = 0 \tag{8}$$

Since Eq. (7) is a first-order, linear differential equation, it can be integrated, to give the UCM model in its single mode integral form [37]:

$$\tau_{xy} = \int_{-\infty}^t \frac{\eta}{\lambda} e^{-\left(\frac{t-t'}{\lambda}\right)} \frac{\partial u}{\partial y} dt' \tag{9}$$

where t, t' and du/dy are respectively, the current time, the past time and the velocity gradient, in which u is a function of y and t'. The shear stress given by Eq. (9) is limited to linear viscoelastic fluids, which comprises motion with infinitesimal deformation gradients. Note also that the differential Eq. (7) for the shear stress component of the UCM fluid, or for each mode, is identical to the corresponding equation for the linear viscoelastic Maxwell model.

2.2. Poisson-Boltzmann equation

When an electrolyte fluid is in contact with a dielectric wall, a spontaneous attraction of counter-ions to the wall surface and corresponding repelling of co-ions takes place near the wall and an ionic charge distribution arises between the wall and the fluid, leading to the formation of an electric double layer (EDL). By assuming that the EDL is thin near each wall, it is possible to consider the two EDL as independent from each other. This assumption is valid provided we are in the dilute regime, where the concentration of solute ions is sufficiently low to prevent ion interactions, therefore the ions follow Boltzmann distribution according to the classical electrostatics theory. This corresponds to a small ionic Péclet number (Pe), defined as Pe = ReSc, where Re and Sc are the Reynolds and Schmidt numbers, respectively. The Schmidt number Sc = eta/(rhoD) is typically of the order of O(10^3) or lower, since the ionic diffusivity (D) of many small ions in water is of the order of O(10^-9) m^2/s and higher. Therefore, in order for Pe <= 1 the Reynolds number must be below O(10^-3) [38]. Note that these are values for steady flow, whereas we are dealing with unsteady flow and defining an oscillatory Reynolds number (Re = rho omega H^2 / eta). Such instantaneous ‘‘oscillatory Reynolds number’’ is equal to the limiting numerical value of Re only twice in the cycle, i.e., by imposing rho omega H^2 / eta = 10^-3 most of the time the flow is in the dilute regime even if Re slightly exceeds this limit value. The induced EDL potential field psi can be expressed by means of a Poisson equation [39]:

$$\nabla^2 \psi = -\frac{\rho_e}{\epsilon} \tag{10}$$

where epsilon denotes the dielectric constant of the solution. The net electric-charge density can be described by a Boltzmann equation [39]:

$$\rho_e = -2n_0 e z \sinh\left(\frac{e z}{k_B T} \psi\right) \tag{11}$$

where  $n_0$  is the ionic density,  $e$  is the elementary electric charge,  $z$  is the valence of the ions,  $k_B$  is the Boltzmann constant, and  $T$  is the absolute temperature. The induced EDL potential field depends only on  $y$ , therefore, Eq. (10) simplifies to:

$$\frac{d^2\psi}{dy^2} = -\frac{\rho_e}{\epsilon} \tag{12}$$

Substituting Eq. (11) into Eq. (12) leads to:

$$\frac{d^2\psi}{dy^2} = \frac{2n_0ez}{\epsilon} \sinh\left(\frac{ez}{k_B T}\psi\right) \tag{13}$$

For small values of  $(ez\psi/k_B T)$  Eq. (13) can be linearized since for small  $x$ ,  $\sinh(x) \cong x$ ; this is termed the Debye–Hückel approximation, which is valid when the electric energy is smaller than the thermal energy and for fluids such as water this limits the zeta potential to about 26 mV at room temperatures [40,41]. This also ensures that ionic finite size effects are negligible, since for dilute solutions, steric effects start to be relevant at zeta potentials of the order of 330 mV for solutions based on water [42]. With this linearization of the hyperbolic sine function, Eq. (13) simplifies to:

$$\frac{d^2\psi}{dy^2} = \kappa^2\psi \tag{14}$$

where  $\kappa^2 = (2n_0e^2z^2/\epsilon k_B T)$  is the Debye–Hückel parameter, and  $\kappa$  represents the inverse of the Debye layer thickness,  $\kappa = 1/\xi$ . Eq. (14) can be integrated for the given boundary conditions,  $\psi(-H) = \psi_1$ ,  $\psi(H) = \psi_2$ , leading to:

$$\psi = \frac{(\psi_2 e^{\kappa H} - \psi_1 e^{-\kappa H})e^{\kappa y} - (\psi_2 e^{-\kappa H} - \psi_1 e^{\kappa H})e^{-\kappa y}}{e^{2\kappa H} - e^{-2\kappa H}} \tag{15}$$

which can be rewritten in compact form as:

$$\psi = \psi_2 (\Omega_1 e^{\kappa y} - \Omega_2 e^{-\kappa y}) \tag{16}$$

where  $\Omega_1 = [e^{\kappa H} - \Pi e^{-\kappa H}]/[2 \sinh(2\kappa H)]$ ,  $\Omega_2 = [e^{-\kappa H} - \Pi e^{\kappa H}]/[2 \sinh(2\kappa H)]$ , and  $\Pi = \psi_1/\psi_2$ . As a consequence, the electric charge density  $\rho_e$  becomes:

$$\rho_e = -\epsilon \kappa^2 \psi_2 (\Omega_1 e^{\kappa y} - \Omega_2 e^{-\kappa y}) \tag{17}$$

Eqs. (16) and (17) are the general formulae for evaluating the potential field, and the net electric charge density, across a 2D channel for any given pair of values of wall zeta potentials,  $\psi_1$  and  $\psi_2$ . Two particular cases are of interest here, as follows:

- *Equal wall zeta potentials:* This is the typical situation, when both walls are made from the same material and the boundary conditions are  $\psi(-H) = \psi(H) = \psi_2$ . Hence  $\Pi = 1$ ,  $\Omega_1 = \sinh(\kappa H)/[\sinh(2\kappa H)]$ ,  $\Omega_2 = -\Omega_1$  and Eqs. (16) and (17) simplify to:

$$\psi = \psi_2 \frac{\cosh(\kappa y)}{\cosh(\kappa H)}, \quad \rho_e = -\epsilon \kappa^2 \psi_2 \frac{\cosh(\kappa y)}{\cosh(\kappa H)} \tag{18}$$

- *Negligible zeta potential at one wall:* This situation arises experimentally when different materials are used in the upper and lower walls with a special deposition treatment in one of the walls to provide a negligible zeta potential there. Here, this is represented by a negligible zeta potential at the lower wall,  $\psi(-H) = 0$ , and a finite potential at the upper wall,  $\psi(H) = \psi_2$ . Therefore  $\Pi = 0$ ,  $\Omega_1 = e^{\kappa H}/[2 \sinh(2\kappa H)]$ ,  $\Omega_2 = e^{-\kappa H}/[2 \sinh(2\kappa H)]$  and Eqs. (16) and (17) simplify to:

$$\psi = \psi_2 \frac{\sinh[\kappa(H+y)]}{\sinh(2\kappa H)}, \quad \rho_e = -\epsilon \kappa^2 \psi_2 \frac{\sinh[\kappa(H+y)]}{\sinh(2\kappa H)} \tag{19}$$

### 2.3. Analytical solution for the multi-mode UCM model

For the multi-mode UCM model the shear stress can be written in its integral form as the sum of  $m$  individual mode contributions, each one given by Eq. (9) [37]:

$$\tau_{xy} = \int_{-\infty}^t \sum_{n=1}^m \frac{\eta_n}{\lambda_n} e^{-(t-t')/\lambda_n} \frac{\partial u}{\partial y} dt' \tag{20}$$

where each mode has its specific polymer viscosity coefficient,  $\eta_n$ , and relaxation time,  $\lambda_n$ . Substituting Eq. (20) into Eq. (2) leads to:

$$\rho \frac{\partial u}{\partial t} = \int_{-\infty}^t \sum_{n=1}^m \frac{\eta_n}{\lambda_n} e^{-(t-t')/\lambda_n} \frac{\partial^2 u}{\partial y^2} dt' + \rho_e E_x \tag{21}$$

We shall now impose an AC electric field in the form,  $E_x = E_0 \cos(\omega t)$ , or  $E_x = \Re(E_0 e^{i\omega t})$  using complex variables, where  $E_0$  is the maximum amplitude of applied potential and  $\omega$  is the frequency of oscillation. The velocity field of the resulting periodic EOF can be written as:

$$u = \Re(u_0 e^{i\omega t}) \tag{22}$$

where  $u_0$  is a complex velocity function in  $y$  to be determined. By substituting both expressions for the electric and velocity fields in Eq. (21), leads to:

$$\begin{aligned} \rho \frac{\partial}{\partial t} (u_0 e^{i\omega t}) &= \int_{-\infty}^t \sum_{n=1}^m \frac{\eta_n}{\lambda_n} e^{-(t-t')/\lambda_n} \frac{\partial^2}{\partial y^2} (u_0 e^{i\omega t'}) dt' + \rho_e (E_0 e^{i\omega t}), \\ i\rho\omega u_0 e^{i\omega t} &= \int_{-\infty}^t \sum_{n=1}^m \frac{\eta_n}{\lambda_n} e^{-(t-t')/\lambda_n} \left[ \frac{\partial^2 u_0}{\partial y^2} e^{i\omega t'} \right] dt' + \rho_e E_0 e^{i\omega t} \end{aligned} \tag{23}$$

Replacing,  $s = t - t'$ ,  $ds / dt' = -1$ , and  $t' = t - s$  leads to [35]:

$$i\rho\omega u_0 e^{i\omega t} = \frac{\partial^2 u_0}{\partial y^2} e^{i\omega t} \int_0^\infty \left( \sum_{n=1}^m \frac{\eta_n}{\lambda_n} e^{-s/\lambda_n} e^{-i\omega s} \right) ds + \rho_e E_0 e^{i\omega t} \tag{24}$$

Integrating the middle term in Eq. (24) with respect to  $s$ , leads to:

$$\int_0^\infty \left( \sum_{n=1}^m \frac{\eta_n}{\lambda_n} e^{-s/\lambda_n} e^{-i\omega s} \right) ds = \sum_{n=1}^m \frac{\eta_n}{1 + i\lambda_n \omega} \tag{25}$$

Substituting Eqs. (25) and (17) into Eq. (24), and dividing both sides by  $e^{i\omega t} \sum_{n=1}^m \frac{\eta_n}{1 + i\lambda_n \omega}$ , and rearranging, leads to:

$$\frac{\partial^2 u_0}{\partial y^2} - \frac{i\rho\omega u_0}{\sum_{n=1}^m \frac{\eta_n}{1 + i\lambda_n \omega}} = \frac{\epsilon \kappa^2 \psi_2 E_0}{\sum_{n=1}^m \frac{\eta_n}{1 + i\lambda_n \omega}} (\Omega_1 e^{\kappa y} - \Omega_2 e^{-\kappa y}) \tag{26}$$

By simple algebra, the summation term  $1/\sum_{n=1}^m [\eta_n/(1 + i\lambda_n \omega)]$  can be written as:

$$\frac{1}{\sum_{n=1}^m \frac{\eta_n}{1 + i\lambda_n \omega}} = \frac{\sum_{n=1}^m \frac{\eta_n}{1 + \lambda_n^2 \omega^2} + i \sum_{n=1}^m \frac{\eta_n \lambda_n \omega}{1 + \lambda_n^2 \omega^2}}{\left( \sum_{n=1}^m \frac{\eta_n}{1 + \lambda_n^2 \omega^2} \right)^2 + \left( \sum_{n=1}^m \frac{\eta_n \lambda_n \omega}{1 + \lambda_n^2 \omega^2} \right)^2} = \frac{A + iB}{A^2 + B^2} \tag{27}$$

where

$$A = \sum_{n=1}^m \frac{\eta_n}{1 + \lambda_n^2 \omega^2}, \quad B = \sum_{n=1}^m \frac{\eta_n \lambda_n \omega}{1 + \lambda_n^2 \omega^2} \tag{28}$$

Substitution of the last term of Eq. (27) into Eq. (26) leads to:

$$\frac{\partial^2 u_0}{\partial y^2} - i\rho\omega u_0 \left( \frac{A + iB}{A^2 + B^2} \right) = \epsilon \kappa^2 \psi_2 E_0 \left( \frac{A + iB}{A^2 + B^2} \right) (\Omega_1 e^{\kappa y} - \Omega_2 e^{-\kappa y}) \tag{29}$$

Eq. (29) can be written in dimensionless form, using the following normalizations:  $\bar{y} = y/H$ ,  $\bar{\kappa} = \kappa H$ ,  $\bar{u}_0 = u_0/u_{sh}$ ,  $Re = \rho\omega H^2/\eta_0$ , and  $\beta_n = \eta_n/\eta_0$  (note that  $\sum_{n=1}^m \beta_n = 1$ ), where  $u_{sh} = -\psi_2 E_0/\eta_0$  is the Smoluchowski velocity based on the upper channel wall zeta potential for the maximum value of the applied potential field,  $E_0$ . Eq. (29) becomes:

$$\frac{\partial^2 \bar{u}_0}{\partial \bar{y}^2} - i \operatorname{Re} \left( \frac{\bar{A} + i \bar{B}}{\bar{A}^2 + \bar{B}^2} \right) \bar{u}_0 = -\bar{\kappa}^2 \left( \frac{\bar{A} + i \bar{B}}{\bar{A}^2 + \bar{B}^2} \right) (\bar{\Omega}_1 e^{\bar{\kappa} \bar{y}} - \bar{\Omega}_2 e^{-\bar{\kappa} \bar{y}}) \quad (30)$$

where

$$\bar{A} = \sum_{n=1}^m \frac{\beta_n}{1 + \lambda_n^2 \omega^2}, \quad \bar{B} = \sum_{n=1}^m \frac{\beta_n \lambda_n \omega}{1 + \lambda_n^2 \omega^2},$$

$$\bar{\Omega}_1 = \frac{e^{\bar{\kappa}} - \Pi e^{-\bar{\kappa}}}{2 \sinh(2\bar{\kappa})}, \quad \bar{\Omega}_2 = \frac{e^{-\bar{\kappa}} - \Pi e^{\bar{\kappa}}}{2 \sinh(2\bar{\kappa})} \quad (31)$$

Eq. (30) represents a complex second-order inhomogeneous ordinary differential equation. For convenience, we replace  $i \operatorname{Re}[(\bar{A} + i \bar{B})/(\bar{A}^2 + \bar{B}^2)]$  by  $(\alpha + i\sigma)^2$ , which results in the following expressions for  $\alpha$  and  $\sigma$ :

$$\alpha = \sqrt{\frac{\operatorname{Re} \left[ \frac{-\bar{B} \pm (\bar{A}^2 + \bar{B}^2)^{1/2}}{\bar{A}^2 + \bar{B}^2} \right]}{2}}, \quad \sigma = \sqrt{\frac{\operatorname{Re} \left[ \frac{\bar{B} \pm (\bar{A}^2 + \bar{B}^2)^{1/2}}{\bar{A}^2 + \bar{B}^2} \right]}{2}} \quad (32)$$

where the  $\pm$  signs in  $\alpha$  and  $\sigma$  must be simultaneously positive, or negative. Now Eq. (30) can be written as (the last term was also written in a more convenient form):

$$\frac{\partial^2 \bar{u}_0}{\partial \bar{y}^2} - (\alpha + i\sigma)^2 \bar{u}_0 = -\bar{\kappa}^2 \left( \frac{\bar{A} + i \bar{B}}{\bar{A}^2 + \bar{B}^2} \right) [(\bar{\Omega}_1 - \bar{\Omega}_2) \cosh(\bar{\kappa} \bar{y}) + (\bar{\Omega}_1 + \bar{\Omega}_2) \sinh(\bar{\kappa} \bar{y})] \quad (33)$$

The general solution of this 2<sup>nd</sup> order inhomogeneous ordinary differential equation (ODE) takes the form:

$$\bar{u}_0 = C_1 e^{(\alpha+i\sigma)\bar{y}} + C_2 e^{-(\alpha+i\sigma)\bar{y}} + A_1 \sinh(\bar{\kappa} \bar{y}) + B_1 \cosh(\bar{\kappa} \bar{y}) + C_3 \quad (34)$$

with the following coefficients:

$$C_1 = -\bar{\kappa}^2 \frac{(\bar{\Omega}_1 + \bar{\Omega}_2) \cosh(\alpha+i\sigma) \sinh(\bar{\kappa}) + (\bar{\Omega}_1 - \bar{\Omega}_2) \sinh(\alpha+i\sigma) \cosh(\bar{\kappa})}{(\alpha^2 - \bar{\kappa}^2 - \sigma^2 + i2\alpha\sigma) \sinh(2\alpha+i2\sigma)} \left( \frac{\bar{A} + i \bar{B}}{\bar{A}^2 + \bar{B}^2} \right),$$

$$C_2 = \bar{\kappa}^2 \frac{(\bar{\Omega}_1 + \bar{\Omega}_2) \cosh(\alpha+i\sigma) \sinh(\bar{\kappa}) - (\bar{\Omega}_1 - \bar{\Omega}_2) \sinh(\alpha+i\sigma) \cosh(\bar{\kappa})}{(\alpha^2 - \bar{\kappa}^2 - \sigma^2 + i2\alpha\sigma) \sinh(2\alpha+i2\sigma)} \left( \frac{\bar{A} + i \bar{B}}{\bar{A}^2 + \bar{B}^2} \right),$$

$$A_1 = \frac{-\bar{\kappa}^2 (\bar{\Omega}_1 + \bar{\Omega}_2)}{\bar{\kappa}^2 - (\alpha+i\sigma)^2} \left( \frac{\bar{A} + i \bar{B}}{\bar{A}^2 + \bar{B}^2} \right), \quad B_1 = \frac{-\bar{\kappa}^2 (\bar{\Omega}_1 - \bar{\Omega}_2)}{\bar{\kappa}^2 - (\alpha+i\sigma)^2} \left( \frac{\bar{A} + i \bar{B}}{\bar{A}^2 + \bar{B}^2} \right), \quad C_3 = 0 \quad (35)$$

Eq. (34) can be rewritten in a compact form:

$$\bar{u}_0 = \Re(\bar{u}_0) + i \Im(\bar{u}_0) \quad (36)$$

with the real and imaginary coefficients given as:

$$\Re(\bar{u}_0) = \Phi_1 \{ \Phi_2 \sinh(\alpha \bar{y}) \sin(\sigma \bar{y}) + \Phi_3 \cosh(\alpha \bar{y}) \cos(\sigma \bar{y}) + \Phi_4 \cosh(\alpha \bar{y}) \sin(\sigma \bar{y}) + \Phi_5 \sinh(\alpha \bar{y}) \cos(\sigma \bar{y}) + \Phi_6 [(\bar{\Omega}_1 + \bar{\Omega}_2) \sinh(\bar{\kappa} \bar{y}) + (\bar{\Omega}_1 - \bar{\Omega}_2) \cosh(\bar{\kappa} \bar{y})] \},$$

$$\Im(\bar{u}_0) = \Phi_1 \{ \Phi_7 \sinh(\alpha \bar{y}) \sin(\sigma \bar{y}) + \Phi_8 \cosh(\alpha \bar{y}) \cos(\sigma \bar{y}) + \Phi_9 \cosh(\alpha \bar{y}) \sin(\sigma \bar{y}) + \Phi_{10} \sinh(\alpha \bar{y}) \cos(\sigma \bar{y}) + \Phi_{11} [(\bar{\Omega}_1 + \bar{\Omega}_2) \sinh(\bar{\kappa} \bar{y}) + (\bar{\Omega}_1 - \bar{\Omega}_2) \cosh(\bar{\kappa} \bar{y})] \} \quad (37)$$

The independent constant coefficients  $\Phi_k$  are presented in Appendix A.

From Eq. (22), written in dimensionless form ( $\bar{u} = u/u_{sh}$ ), we can now obtain the expression for the EOF velocity field:

$$\bar{u} = \Re(\bar{u}_0 e^{i\omega t}) = \Re(\bar{u}_0) \cos(\omega t) - \Im(\bar{u}_0) \sin(\omega t) \quad (38)$$

Similarly, when imposing an external potential field of the form  $E_x = E_0 \sin(\omega t) = \Im(E_0 e^{i\omega t})$ , the dimensionless velocity for this sine wave external forcing would be:

$$\bar{u} = \Im(\bar{u}_0 e^{i\omega t}) = \Re(\bar{u}_0) \sin(\omega t) + \Im(\bar{u}_0) \cos(\omega t) \quad (39)$$

The previous expressions represent the velocity field when an external applied potential field of the form of a cosine or a sine wave is imposed in a microchannel with different wall zeta potentials, respectively. Next, we analyse the two above-mentioned particular solutions corresponding to the cases when both walls have the same zeta potential and when one of the walls has a negligible zeta potential, as follows:

- *Equal wall zeta potentials:* in this case, the real and imaginary terms of  $\bar{u}_0$  are respectively expressed as:

$$\Re(\bar{u}_0 \text{ EZP}) = \Theta_1 [\Theta_2 \cosh(\alpha \bar{y}) \cos(\sigma \bar{y}) + \Theta_3 \sinh(\alpha \bar{y}) \sin(\sigma \bar{y}) + \Theta_4 \cosh(\bar{\kappa} \bar{y})],$$

$$\Im(\bar{u}_0 \text{ EZP}) = \Theta_1 [\Theta_5 \cosh(\alpha \bar{y}) \cos(\sigma \bar{y}) + \Theta_6 \sinh(\alpha \bar{y}) \sin(\sigma \bar{y}) + \Theta_7 \cosh(\bar{\kappa} \bar{y})] \quad (40)$$

where the subscript EZP denotes "equal zeta potential" and the constant coefficients  $\Theta_k$  are defined in Appendix B.

The resulting velocity field generated by an externally imposed potential field of the form  $E_x = E_0 \cos(\omega t)$  is given by:

$$\bar{u} = \Re(\bar{u}_0 \text{ EZP}) \cos(\omega t) - \Im(\bar{u}_0 \text{ EZP}) \sin(\omega t) \quad (41)$$

and when the applied external potential field is given by  $E_x = E_0 \sin(\omega t)$ , the resulting velocity field is:

$$\bar{u} = \Re(\bar{u}_0 \text{ EZP}) \sin(\omega t) + \Im(\bar{u}_0 \text{ EZP}) \cos(\omega t) \quad (42)$$

- *Negligible zeta potentials at the lower wall:* in this special case, the real and imaginary terms of  $\bar{u}_0$  are given by:

$$\Re(\bar{u}_0 \text{ NZP}) = \Xi_1 \{ \Xi_2 \cosh(\alpha \bar{y}) \sin(\sigma \bar{y}) + \Xi_3 \sinh(\alpha \bar{y}) \cos(\sigma \bar{y}) + \Xi_4 \sinh(\alpha \bar{y}) \sin(\sigma \bar{y}) + \Xi_5 \cosh(\alpha \bar{y}) \cos(\sigma \bar{y}) + \Xi_6 \{ \cosh(\bar{\kappa}) \sinh(\bar{\kappa} \bar{y}) + \sinh(\bar{\kappa}) \cosh(\bar{\kappa} \bar{y}) \} \},$$

$$\Im(\bar{u}_0 \text{ NZP}) = \Xi_1 \{ \Xi_7 \cosh(\alpha \bar{y}) \sin(\sigma \bar{y}) + \Xi_8 \sinh(\alpha \bar{y}) \cos(\sigma \bar{y}) + \Xi_9 \sinh(\alpha \bar{y}) \sin(\sigma \bar{y}) + \Xi_{10} \cosh(\alpha \bar{y}) \cos(\sigma \bar{y}) + \Xi_{11} \{ \cosh(\bar{\kappa}) \sinh(\bar{\kappa} \bar{y}) + \sinh(\bar{\kappa}) \cosh(\bar{\kappa} \bar{y}) \} \} \quad (43)$$

where the subscript NZP stands for "negligible zeta potential" and the constant coefficients  $\Xi_k$  are defined in Appendix C.

The resulting velocity field generated by an externally imposed potential field of the form  $E_x = E_0 \cos(\omega t)$  is given by:

$$\bar{u} = \Re(\bar{u}_0 \text{ NZP}) \cos(\omega t) - \Im(\bar{u}_0 \text{ NZP}) \sin(\omega t) \quad (44)$$

and when the applied external potential field is given by  $E_x = E_0 \sin(\omega t)$ , the resulting velocity field is:

$$\bar{u} = \Re(\bar{u}_0 \text{ NZP}) \sin(\omega t) + \Im(\bar{u}_0 \text{ NZP}) \cos(\omega t) \quad (45)$$

#### 2.4. Analytical solution for generic periodic forcings

In general, assuming the applied potential field has a cyclic nature of period  $T$ , it can be written as:

$$E_x(t) = E_0 f(\cos(\omega_j t) + i \sin(\omega_j t)) \quad (46)$$

with  $\omega_j = 2\pi j/T$ .

Let the function  $E_x(t)$  be defined in the range  $-T/2 \leq t \leq T/2$ , so that its Fourier series can be represented by:

$$E_x(t) = E_0 \left[ a_0 + \sum_{j=1}^{\infty} a_j \cos(\omega_j t) + b_j \sin(\omega_j t) \right] \quad (47)$$

The coefficients  $a_0$ ,  $a_j$ , and  $b_j$  can be computed as:

$$a_0 = \frac{1}{T} \int_{-T/2}^{T/2} E_x(t) dt, \quad a_j = \frac{2}{T} \int_{-T/2}^{T/2} E_x(t) \cos(\omega_j t) dt,$$

$$b_j = \frac{2}{T} \int_{-T/2}^{T/2} E_x(t) \sin(\omega_j t) dt \quad (48)$$

Due to the linearity of the governing equations and of the boundary conditions, the resulting velocity field induced by this generic electric potential can thus be written as a linear combination of the velocity fields generated by each of the terms of the Fourier series, so that it has the general form:

$$\bar{u} = \frac{-\eta_0}{\epsilon \psi_2 E_0} u = a_0 \Re(\bar{u}_0) + \sum_{j=1}^{\infty} \{ a_j [\Re(\bar{u}_0) \cos(\omega_j t) - \Im(\bar{u}_0) \sin(\omega_j t)] + b_j [\Re(\bar{u}_0) \sin(\omega_j t) + \Im(\bar{u}_0) \cos(\omega_j t)] \} \quad (49)$$

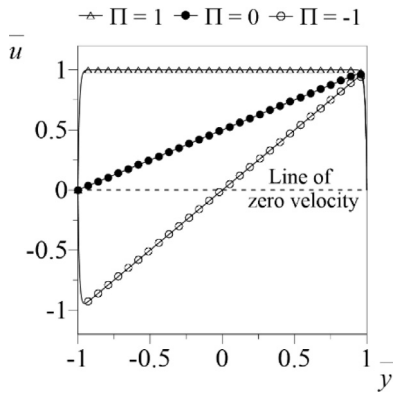


Fig. 2. Profiles of the normalized streamwise velocity component for a Newtonian fluid with  $\Pi = \psi_1/\psi_2 = -1, 0$ , and  $1$  at  $Re = 0.001$ ,  $\bar{\kappa} = 100$ ,  $\omega t = 0$  and  $m = 1$ .

### 3. Results and discussion

In the previous section, the analytical solutions were obtained for oscillatory flow of a viscoelastic fluid, described by the multi-mode Maxwell model under the sole influence of an oscillating electro-osmosis driving force, when the channel walls are characterized by asymmetric or symmetric zeta potentials. In this section the case of single mode model ( $m = 1$ ) is considered, unless otherwise stated. The main objective here is to discuss the influences of selected parameters on the oscillatory shear flow to provide a better understanding about the practical use of SAOSEO, in particular to investigate the flow regime where the velocity profile is linear and has a magnified amplitude of oscillation. Such characteristics are necessary and useful, respectively, if one wishes to use this flow as a measuring tool to characterize the linear rheological properties of viscoelastic fluids, such as the storage ( $G'$ ) and loss ( $G''$ ) moduli. Liu et al. [35] has also used the single mode UCM model to investigate periodically forced electro-osmotic flow, but they aimed at generally characterizing the velocity profiles and volumetric flow rate as a function of the oscillating Reynolds number, EDL thickness and normalized relaxation time (Deborah number). Even though our general flow features are similar for a single mode, the focus of our discussion is quite different and in addition we will also look at a two-mode model.

A general formulation for the dimensionless velocity profile,  $\bar{u} = u/u_{sh}$ , is given by Eq. (38) as a function of dimensionless time,  $\omega t$ , and the dimensionless channel transverse coordinate,  $\bar{y}$ . Eq. (38) can be further simplified for simple cases, and we consider the limiting cases of equal wall zeta potentials (EZP) and of negligible zeta potential (NZP) in the lower wall, given by Eqs. (41) and (44), respectively. Eqs. (38), (41) and (44), result from an externally applied potential field of the form  $E_x = E_0 \cos(\omega t)$ , which depends on the following dimensionless parameters:  $\bar{\kappa}$ ,  $\omega t$ ,  $\lambda_n \omega$ ,  $Re$ ,  $\Pi$  and  $\beta_n$ , where  $n$  represents the mode number. Using the weighted-averaged relaxation time  $\lambda = \sum_{n=1}^m \lambda_n \beta_n$ , where  $n \neq$  solvent [43], we define the Deborah number,  $De = \lambda \omega$  [44], which is a fundamental independent dimensionless number in this flow. Additional dimensionless quantities that help to understand the flow physics are the oscillatory Reynolds number ( $Re = \rho \omega H^2 / \eta_0$ ), and in particular the viscoelastic Mach number ( $M = \sqrt{Re De}$ ), which gives an indication of the propagation of shear waves (in elastic fluids at rest shear waves propagate with constant velocity,  $c = \sqrt{\eta / \rho \lambda}$ ).

For purely driven electro-osmotic flow of a Newtonian fluid ( $m = 1$ ,  $\lambda = 0$ ), Fig. 2 shows the influence of  $\Pi$  on the normalized velocity profiles, plotted as a function of the dimensionless transverse coordinate. The results are calculated from Eq. (38) for  $\Pi = -1, 0$ , and  $1$ , under the same flow conditions of  $Re = 0.001$ ,  $\bar{\kappa} = 100$ , and  $\omega t = 0$ . The cases  $\Pi = 1$  and  $\Pi = -1$  refer to equal and opposite wall zeta potentials at both upper and lower walls, respectively, while  $\Pi = 0$  refers to the case with a neutral

(no charge) lower wall. As expected, Fig. 2 shows that  $\Pi = 1$  results in a symmetric velocity profile, while for  $\Pi = -1$  and  $\Pi = 0$  anti-symmetric and asymmetric profiles are found, respectively.

The results shown in Figs. 3–6 are calculated using Eq. (44), and correspond to the case of  $\Pi = 0$  (NZP) and  $m = 1$  (one mode), whereas Fig. 7 pertains to  $m = 2$  (more specifically, a Newtonian solvent mode plus one viscoelastic mode).

Fig. 3 illustrates the oscillatory flow behavior at  $\omega t = 0$ , for a Newtonian fluid on the left-hand side and for a viscoelastic fluid ( $\lambda \omega = 5$ ) on the right-hand side, with  $Re$  varying from 0.001 to 10 and  $\bar{\kappa}$  varying from 5 to 200. Since the fluid on the right plot is elastic, the viscoelastic Mach number can be computed and varies from  $M = 0.07$  to  $M = 7.1$ , here due to the variation of  $Re$ . Note that when  $Re$  exceeds the range of validity associated with the existence of a thin EDL, discussed in Section 2.2, this solution, assuming the existence of a thin EDL and the validity of a Boltzmann distribution of ions, no longer shows linearly behaved velocity profiles.

To further illustrate the influence of Reynolds number, we show in Fig. 3 that for small  $Re$  (e.g.  $Re = 0.001$ ) there are no detectable differences between the Newtonian (Fig. 3-(A-i)) and viscoelastic profiles (Fig. 3-(A-ii)), regardless of the value of  $\bar{\kappa}$ , but provided  $\bar{\kappa}$  is the same in both cases. In addition, as the value of  $\bar{\kappa}$  increases and the Debye layer becomes progressively thinner the velocity profiles across the channel become more linear. Furthermore, for the Newtonian fluid, Fig. 3-(B-i) to 3-(D-i) show that at low  $Re$  oscillations are weak due to viscous dampening, but oscillatory behavior is slowly enhanced as  $Re$  increases and this is accompanied by a gradual decay in the amplitude of the normalized velocity profile. In contrast, for the viscoelastic fluid ( $\lambda \omega = 5$ ) significant changes take place as  $Re$  and  $M$  progressively increase from  $Re = 0.01$  and  $M = 0.22$  in Fig. 3-(B-ii) to  $Re = 10$  and  $M = 7.1$  in Fig. 3-(D-ii). A wave behavior is clearly perceived to form already at  $(Re, M) = (1, 2.2)$  and as the viscoelastic Mach number further increases the flow becomes largely dominated by elastic waves rather than by viscous effects with the amplitude of the waves and their spatial frequency increasing with  $Re$  (this is shown as a compression of the waves towards the plate with higher zeta potential). Furthermore, as  $Re$  increases to  $Re = 10$  the amplitude of the propagating waves decay faster on moving away from the high zeta potential plate ( $\bar{y} = 1$ ), because viscous diffusion is not sufficiently fast to transport information towards the other wall (note that  $Re$  is proportional to the oscillation frequency). In contrast, at lower  $Re$  the elastic waves have a more uniform amplitude, because viscous diffusion can act more effectively across the whole channel. This has similarities to what was observed by Cruz and Pinho [44] in their investigation of Stokes' second problem with UCM fluids, who showed that the penetration depth ( $y_p$ ) varies in inverse proportion to the Reynolds number very much as the boundary layer thickness in laminar boundary layers for Newtonian fluid flows.

As mentioned above, at low Reynolds number the normalized velocity profiles for Newtonian and viscoelastic ( $\lambda \omega = 5$ ) fluids are linear in  $\bar{y}$ , but for the latter case this is only true at low  $De$  (low viscoelastic Mach number). As shown in Fig. 4, as  $\lambda \omega$  progressively increases very slight deviations from linearity gradually appear for  $Re = 0.001$  (cf. left-hand side), and become more intense as the Reynolds number increases, even though those deviations are still small at  $Re = 0.01$  (cf. right-hand side (RHS)). The deviation from linearity shown on the RHS progresses from the high zeta potential wall and is stronger the higher the value of  $\lambda \omega$ , regardless of the value of  $\bar{\kappa}$ . In order to recover linear behavior, as the fluid elasticity is increased (fluid relaxation time increased) the oscillation frequency must be concomitantly reduced.

As discussed in Section 2.2, the critical Reynolds number associated with the validity of a ionic Boltzmann distribution is  $Re_{cr} \approx 0.001$ , but for a Newtonian fluid the velocity profile would cease to behave linearly for  $Re_{cr} \approx 0.01$  if the ionic Péclet number did not impose a limit. For viscoelastic fluids, the flow is controlled also by the fluid elasticity, here quantified by  $\lambda \omega$  or  $M$ . Viscoelasticity also affects the linearity of the flow response so we need to consider for this fluid two additional

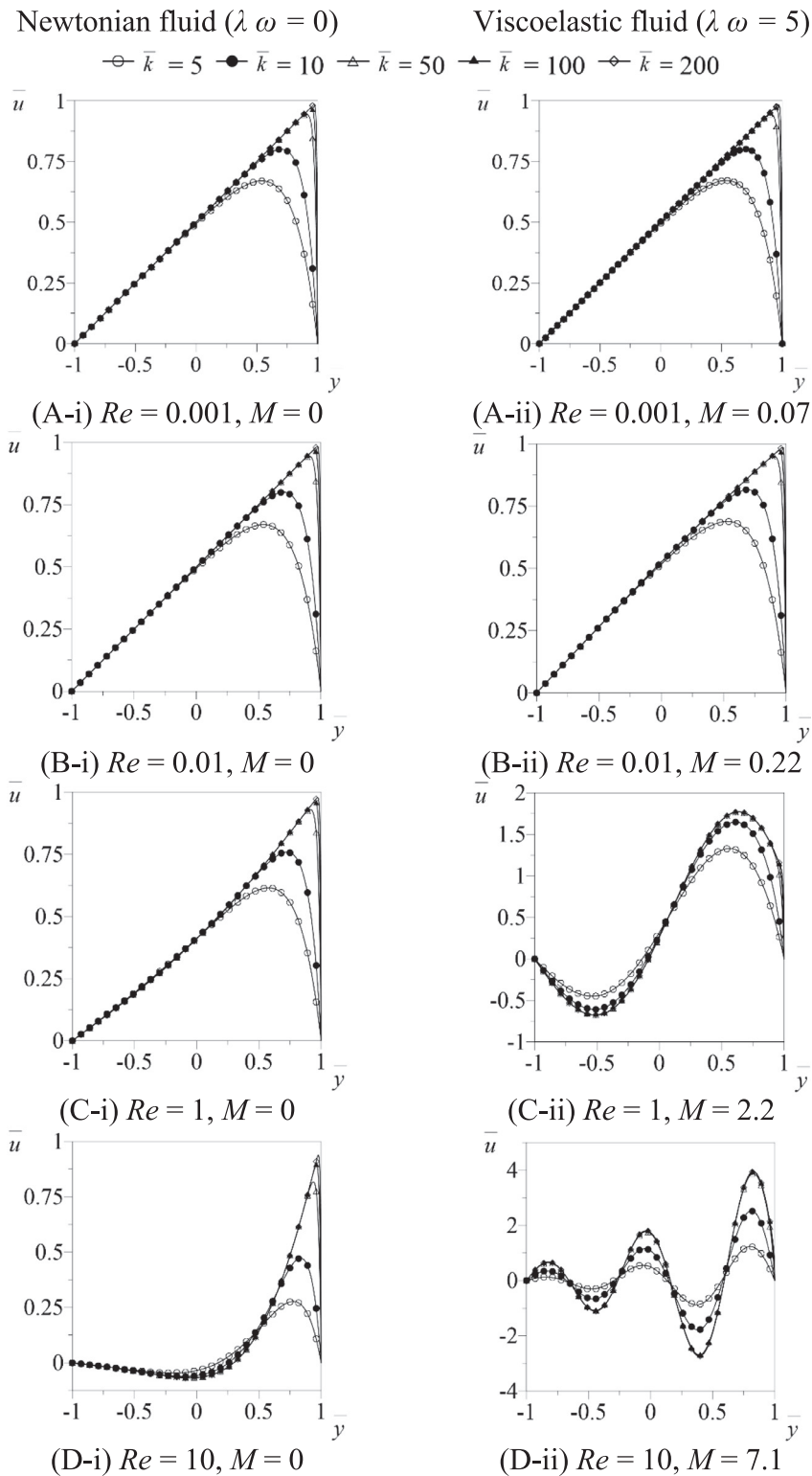
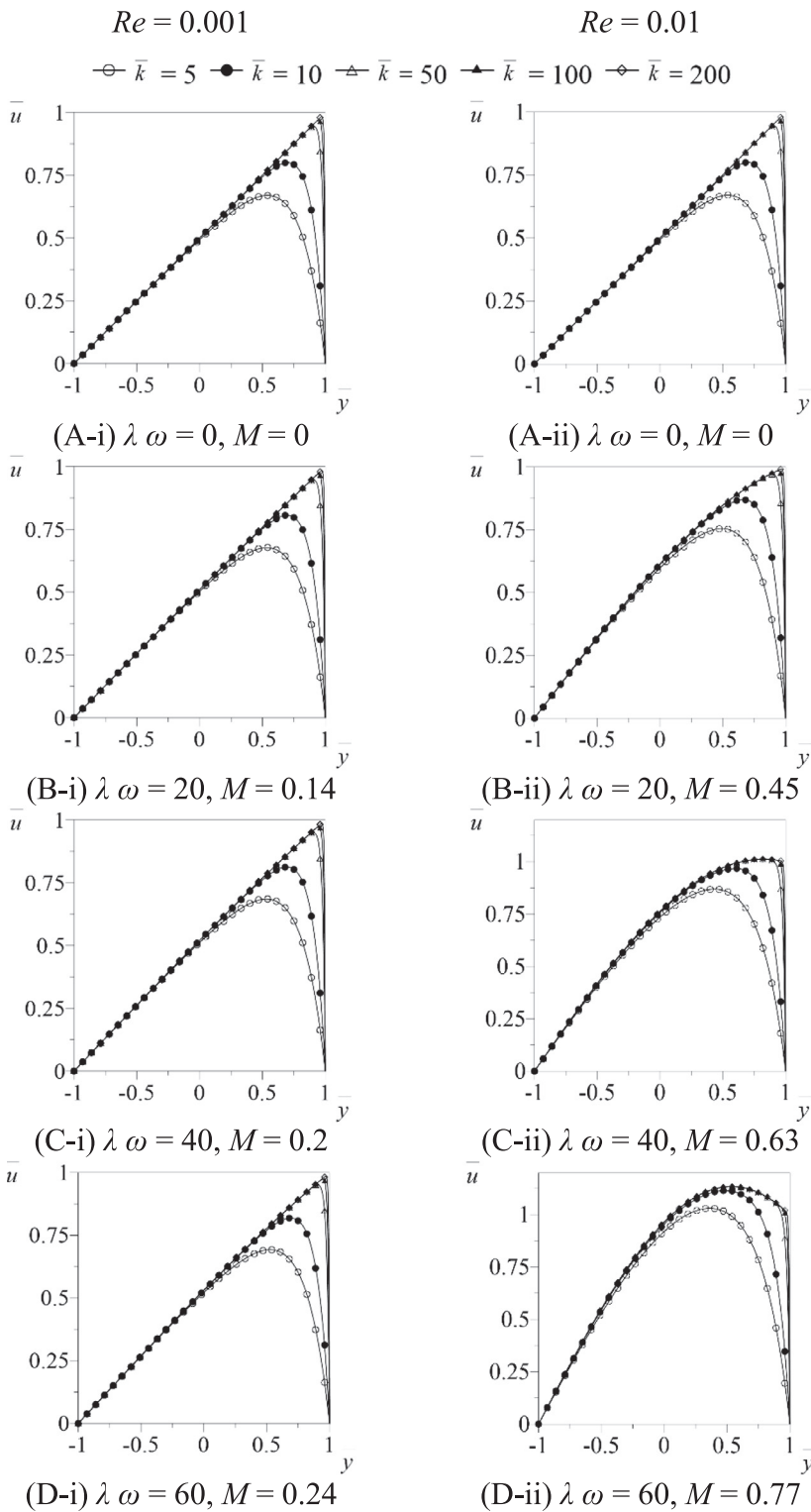


Fig. 3. Profiles of the normalized velocity for a Newtonian fluid (left-hand side) and a viscoelastic fluid,  $De = \lambda\omega = 5$  (right-hand side) for  $\omega t = 0, \Pi = 0$  and  $m = 1$ , as a function of  $\bar{k}$ , Reynolds ( $Re$ ) and viscoelastic Mach ( $M$ ) numbers: (A-i)  $Re = 0.001, M = 0$ ; (B-i)  $Re = 0.01, M = 0$ ; (C-i)  $Re = 1, M = 0$ ; (D-i)  $Re = 10, M = 0$  and (A-ii)  $Re = 0.001, M = 0.07$ ; (B-ii)  $Re = 0.01, M = 0.22$ ; (C-ii)  $Re = 1, M = 2.2$  and (D-ii)  $Re = 10, M = 7.1$

critical limits: the critical Deborah number ( $De_{cr}$ ) and the critical viscoelastic Mach number ( $M_{cr}$ ) above which the velocity ceases to be linear. Since all effects are coupled, for  $Re_{cr} \approx 0.01$  the corresponding critical Deborah and viscoelastic Mach numbers are  $De_{cr} \approx 10$  and  $M_{cr} \approx 0.32$ , whereas for the critical  $Re_{cr} \approx 0.001$  we have  $De_{cr} \approx 100$  and the same  $M_{cr} \approx 0.32$ . The critical values of  $De$  were determined by imposing a maximum deviation of 10% to the normalized velocity at the channel centerline ( $\bar{y} = 0$ ) in relation to the Newtonian linear veloc-

ity profile at the instant  $\omega t = 0$ , the profile in Fig. 4-(A-i) as  $\bar{k} \rightarrow \infty$ . The critical values of  $M$  are obtained from the following definition:  $M_{cr} = \sqrt{Re_{cr} De_{cr}}$ . Incidentally, for those two Reynolds numbers, the variation of  $De_{cr}$  with the value of the maximum deviation ( $\Delta$  in [%]) criterion is approximately linear, i.e.,  $De_{cr} \approx 0.01 \Delta / Re$  or  $M_{cr} \approx 0.1 \sqrt{\Delta}$ . Hence, to design a micro-rheometer for SAOSEO, we should not exceed these critical limits when using either Newtonian ( $Re_{cr}$ ), or viscoelastic fluids ( $Re_{cr}, M_{cr}$  and  $De_{cr}$ ) in order to obtain the desired flow field.



**Fig. 4.** Profiles of the normalized velocity components for different Deborah numbers ( $\lambda\omega$ ), viscoelastic Mach ( $M$ ) numbers and  $\bar{k}$  values, at Reynolds number  $Re = 0.001$  (left-hand side) and  $Re = 0.01$  (right-hand side), at instant  $\omega t = 0$  with  $\Pi = 0$  and  $m = 1$ : (A-i)  $\lambda\omega = 0, M = 0$ ; (B-i)  $\lambda\omega = 20, M = 0.14$ ; (C-i)  $\lambda\omega = 40, M = 0.2$  and (D-i)  $\lambda\omega = 60, M = 0.24$ ; (A-ii)  $\lambda\omega = 0, M = 0$ ; (B-ii)  $\lambda\omega = 20, M = 0.45$ ; (C-ii)  $\lambda\omega = 40, M = 0.63$  and (D-ii)  $\lambda\omega = 60, M = 0.77$ .

Fig. 5 presents the variation of the normalized velocity profile along a full cycle of oscillation ( $\omega t$  varies from 0 to  $2\pi$ ), for  $\bar{k} = 100, \Pi = 0$  and  $Re = \{ 0.001, 10 \}$ . Newtonian and viscoelastic fluids have plots on the left and right-hand-side, respectively. At low  $Re$ , here represented by  $Re = 0.001$ , Fig. 5-(A) shows that both fluids fluctuate in a linear manner, but the viscoelastic fluid oscillates with a higher amplitude which changes with  $\omega t$  especially when  $\omega t = \pi/2$  and  $3\pi/2$ , while the Newtonian fluid oscillates with a lower amplitude and less detectable differences with the variation of  $\omega t$ . Fig. 5-(B), pertaining to  $Re = 10$ ,

already shows that even though the maximum amplitude of oscillation near the wall is the same as for the lower  $Re = 0.001$  case, both fluids fluctuate now in a non-linear manner, with the viscoelastic fluid oscillating more intensively due to the fluid elasticity (i.e. the waves decay very slowly with distance to the wall), while the waves of the Newtonian fluid are quickly dampened on going from the EDL wall to the wall with a negligible zeta potential. When critical values of the relevant dimensionless parameters are exceeded, this figure clearly shows that this set-up should not be used for the purpose of SAOSEO.

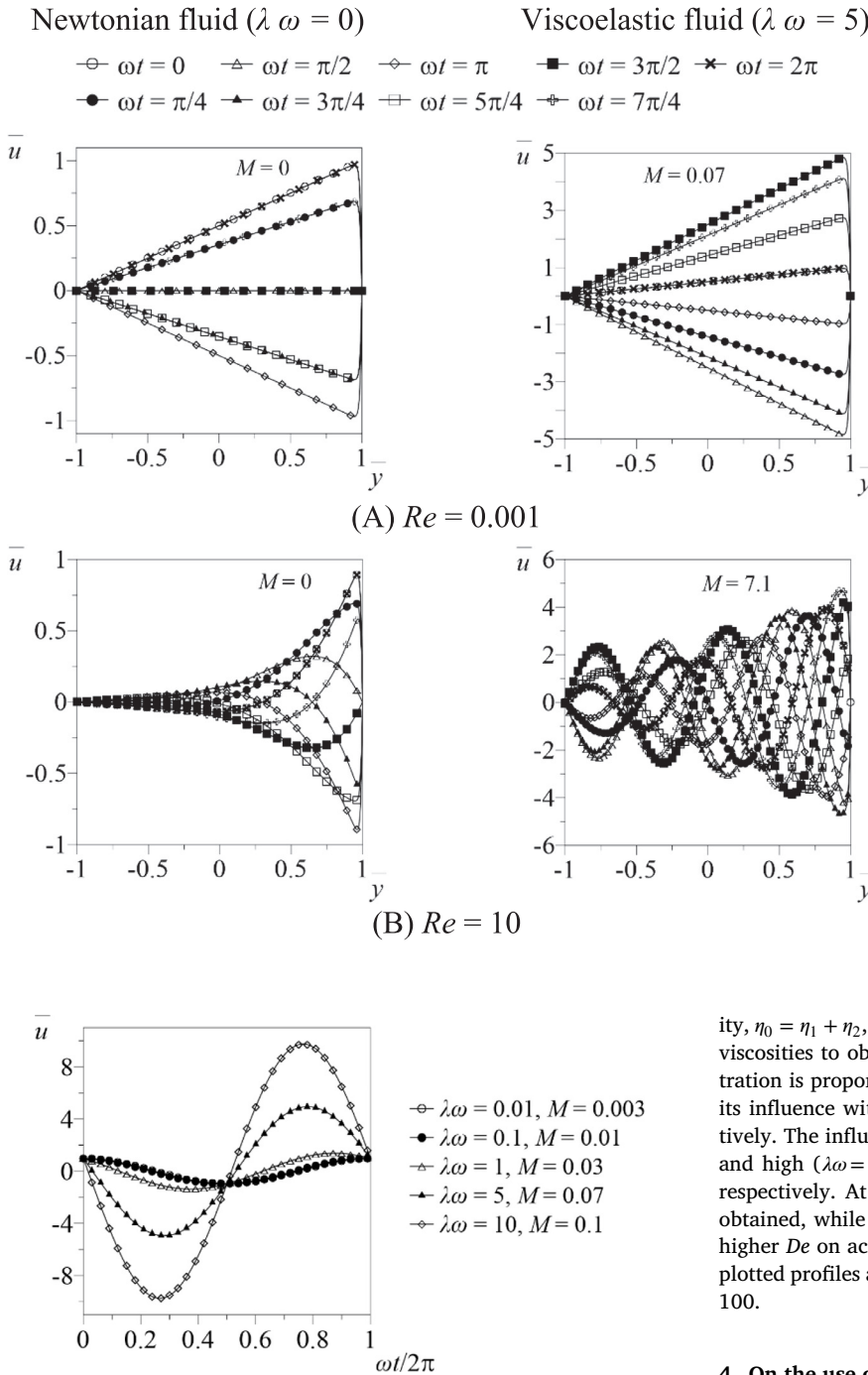


Fig. 5. Profiles of the normalized velocity for a Newtonian fluid (left-hand side) and a viscoelastic fluid,  $De = \lambda\omega = 5$  (right-hand side) for  $\bar{\kappa} = 100$ ,  $\Pi = 0$ ,  $m = 1$ , and as a function of  $\omega t$  and Reynolds number: (A)  $Re = 0.001$ , (B)  $Re = 10$ .

Fig. 6. Variation of the normalized velocity at  $\bar{y} = 0.95$  with  $\omega t/2\pi$  for  $Re = 0.001$ ,  $\bar{\kappa} = 100$ ,  $\Pi = 0$ ,  $m = 1$  and as a function of  $De = \lambda\omega$ .

Fig. 6 shows the influence of varying  $\lambda\omega$  from 0.01 to 10 on the normalized velocity profile for one full cycle at the position  $\bar{y} = 0.95$ , i.e. close to the high zeta potential surface for  $Re = 0.001$ ,  $\bar{\kappa} = 100$ , and  $\Pi = 0$ . The amplitude of the velocity profile increases with  $\lambda\omega$ , and the velocity becomes progressively out-of phase with the imposed electric potential, due to the conspicuous increase in the fluid elasticity.

The addition of even a small amount of polymer to an otherwise Newtonian fluid alters significantly the fluid rheology which is a function of fluid concentration. In Fig. 7 we consider the simplest polymer solution, a two-mode fluid, where the first mode corresponds to the Newtonian solvent ( $\lambda_1 = 0$  and viscosity  $\eta_1$ ) and the second mode to the polymer additive with relaxation time  $\lambda_2$  and viscosity  $\eta_2$ . The total viscos-

ity,  $\eta_0 = \eta_1 + \eta_2$ , is kept constant, while varying the solvent and polymer viscosities to obtain solutions at different concentrations. The concentration is proportional to  $1 - \beta_1 = \eta_2 / (\eta_1 + \eta_2)$  and in the plots we assess its influence with values of  $1 - \beta_1 = 0.1, 0.2, 0.3, 0.4$  and  $0.5$ , respectively. The influence of concentration is investigated for low ( $\lambda\omega = 0.1$ ) and high ( $\lambda\omega = 5$ ) Deborah numbers, as shown in Fig. 7-(A) and (B), respectively. At low  $De$  identical Newtonian-like velocity profiles are obtained, while significant variation in the amplitude was realized for higher  $De$  on account of the elastic amplification of elastic waves. The plotted profiles are all at the instant of  $\omega t = 0$ ,  $Re = 0.001$ ,  $\Pi = 0$ , and  $\bar{\kappa} = 100$ .

#### 4. On the use of electro-osmosis for SAOS rheology

The previous section discussed the analytical results obtained by inspection of the velocity profiles as a function of relevant quantities ( $\bar{\kappa}$ ,  $\omega t$ ,  $\lambda_n\omega$ ,  $Re$ ,  $M$ ,  $\Pi$ ) and defined critical numbers beyond which the velocity field is no longer linear in  $\bar{y}$ . This section discusses the development of a microchannel rheometer for SAOS, but working on the principles of EOF as a measuring tool.

On characterizing the linear viscoelastic rheological properties of non-Newtonian fluids by means of small amplitude oscillatory electro-osmotic shear flow (henceforth denoted SAOSEO), we quantify specific SAOSEO storage ( $G'$ ) and loss ( $G''$ ) moduli from which it will be possible to determine the spectra of relaxation times ( $\lambda_n$ ) and of viscosity coefficients ( $\eta_n$ ) as in standard SAOS. This requires SAOSEO to be imposed under the operational conditions of very small  $Re$  ( $Re < 0.001$ ), large  $\bar{\kappa}$  (e.g.  $\bar{\kappa} \geq 100$ ) and low  $De$  ( $\lambda\omega \leq 100$ ), thus corresponding to low  $M$  ( $M \leq 0.32$ ) to ensure a homogenous shear flow, with a

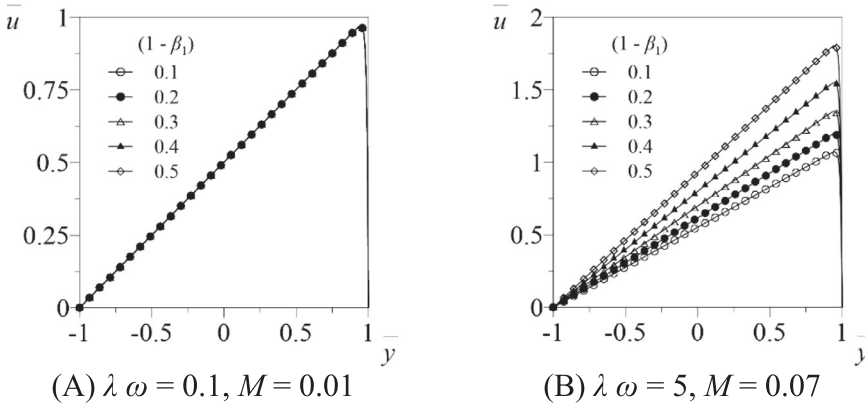


**Fig. 7.** Effect of  $1 - \beta_1 = \eta_2/(\eta_1 + \eta_2)$  on the profiles of the normalized velocity for a two-mode polymer solution (mode 1: Newtonian solvent, mode 2: polymer additive) at  $Re = 0.001$ ,  $\Pi = 0$ ,  $\bar{\kappa} = 100$  at instant  $\omega t = 0$  for Deborah ( $\lambda\omega$ ) and Mach ( $M$ ) numbers of: (A)  $\lambda\omega = 0.1$ ,  $M = 0.01$  and (B)  $\lambda\omega = 5$ ,  $M = 0.07$ .

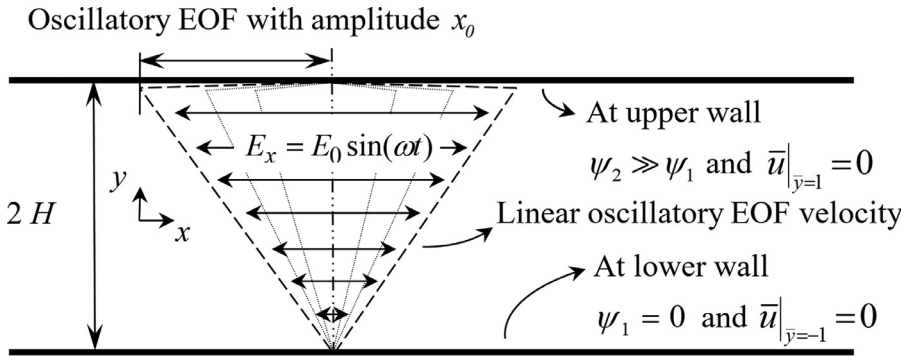


**Fig. 8.** Schematic diagram illustrating small amplitude oscillatory electro-osmotic flow (SAOSEO) under operating conditions of very small  $Re$  and large  $\bar{\kappa}$ , leading to a flow with similar characteristics to that of SAOS in rotational shear.

time-dependent linear velocity profile. The fluid contained inside a straight microchannel is forced by an externally imposed potential field of the form  $E_x = E_0 \sin(\omega t)$  between the microchannel inlet and outlet. The fluid inside the microchannel oscillates in a sinusoidal mode at an angular frequency  $\omega$ , with an amplitude varying with time  $t$ , as illustrated in Fig. 8, in a fashion that is similar to what was already described in Fig. 5-(A) at small  $Re = 0.001$  and high  $\bar{\kappa} = 100$  for both Newtonian and viscoelastic fluids. The velocity profile across the channel is linear, except in the vicinity of the upper wall.

The profile of the normalized velocity, schematically shown in Fig. 8 for negligible zeta potential at the lower wall,  $\Pi = 0$ , is given in Eq. (45), but by imposing now the conditions of a very small  $Re$  and a large  $\bar{\kappa}$ , that equation can be further simplified. Indeed, the second term on the left hand-side of the momentum Eq. (30),  $i Re[(\bar{A} + i\bar{B})/(\bar{A}^2 + \bar{B}^2)]$ , can be neglected so that by integrating Eq. (30) leads to (we skip the details for conciseness):

$$\bar{u}_0 = \Re(\bar{u}_0) + i\Im(\bar{u}_0) \quad (50)$$

where the real and the imaginary terms of the complex velocity function are given as:

$$\begin{aligned} \Re(\bar{u}_0) &= \frac{1}{2} \left( \frac{\bar{A}}{\bar{A}^2 + \bar{B}^2} \right) \left\{ (1 + \Pi) \left[ 1 - \frac{\cosh(\bar{\kappa}\bar{y})}{\cosh(\bar{\kappa})} \right] + (1 - \Pi) \left[ \bar{y} - \frac{\sinh(\bar{\kappa}\bar{y})}{\sinh(\bar{\kappa})} \right] \right\}, \\ \Im(\bar{u}_0) &= \frac{1}{2} \left( \frac{\bar{B}}{\bar{A}^2 + \bar{B}^2} \right) \left\{ (1 + \Pi) \left[ 1 - \frac{\cosh(\bar{\kappa}\bar{y})}{\cosh(\bar{\kappa})} \right] + (1 - \Pi) \left[ \bar{y} - \frac{\sinh(\bar{\kappa}\bar{y})}{\sinh(\bar{\kappa})} \right] \right\} \end{aligned} \quad (51)$$

For large  $\bar{\kappa}$ , Eq. (51) can be further simplified by dropping the sinh and cosh, which are responsible for the sharp velocity gradient near the upper wall due to the EDL thickness effect, leading to:

$$\begin{aligned} \Re(\bar{u}_0) &= \left( \frac{\bar{A}}{\bar{A}^2 + \bar{B}^2} \right) \left\{ \frac{(1 + \Pi) + \bar{y}(1 - \Pi)}{2} \right\}, \\ \Im(\bar{u}_0) &= \left( \frac{\bar{B}}{\bar{A}^2 + \bar{B}^2} \right) \left\{ \frac{(1 + \Pi) + \bar{y}(1 - \Pi)}{2} \right\} \end{aligned} \quad (52)$$

So, as a result of imposing an external potential field of the form  $E_x = E_0 \sin(\omega t)$ , the ensuing velocity field is a function of time and of the dependent variable  $\bar{y}$  in the following way:

$$u = u_{sh} \frac{(1 + \Pi) + \bar{y}(1 - \Pi)}{2} \left\{ \frac{\bar{A}}{\bar{A}^2 + \bar{B}^2} \sin(\omega t) + \frac{\bar{B}}{\bar{A}^2 + \bar{B}^2} \cos(\omega t) \right\} \quad (53)$$

where the first term of Eq. (53) is in-phase with the imposed potential  $E_x$  (viscous response) and the second term is out-of-phase (elastic response). Alternatively, the previous equation can be written as:

$$u = u_{sh} \frac{(1 + \Pi) + \bar{y}(1 - \Pi)}{2} \frac{1}{\sqrt{\bar{A}^2 + \bar{B}^2}} \sin(\omega t + \phi) \quad (54)$$

where  $\phi$  represents the phase difference between the imposed potential and the resulting velocity profile, and it is defined as:

$$\phi = \cos^{-1} \left( \frac{\bar{A}}{\sqrt{\bar{A}^2 + \bar{B}^2}} \right) = \sin^{-1} \left( \frac{\bar{B}}{\sqrt{\bar{A}^2 + \bar{B}^2}} \right) \quad (55)$$

For a purely viscous fluid  $\phi = 0$ , while for a purely elastic material  $\phi = \pi/2$  (in SAOS  $\delta$  represents the phase difference between the imposed strain and the resulting shear stress, note that  $\delta = \pi/2 - \phi$ ).

The position of tracer particles can also be determined from the integration of the velocity profile,  $x - x_0 = \int_{t_0}^t u dt$ , resulting in:

$$x = x_0 - u_{sh} \frac{(1 + \Pi) + \bar{y}(1 - \Pi)}{2\omega\sqrt{\bar{A}^2 + \bar{B}^2}} \left\{ \cos(\omega t + \phi) - \cos(\omega t_0 + \phi) \right\} \quad (56)$$

The maximum displacement of a particle over a full cycle of oscillation is given by:

$$\Delta x_{max} = u_{sh} \frac{(1 + \Pi) + \bar{y}(1 - \Pi)}{\omega\sqrt{\bar{A}^2 + \bar{B}^2}} \quad (57)$$

In practice, the SAOSEO test can be easily implemented in straight microfluidic channels, by measuring the velocity using a particle image velocimetry (PIV) system or by tracing the displacement of individual

tracer particles using particle tracking velocimetry (PTV). To evaluate  $u_{sh}$  and  $\Pi$  for an applied  $E_0$  potential, we need to know the zeta potentials of the walls (besides  $\epsilon$  and  $\eta_0$ ), which are not easily available. Alternatively, we propose a simple technique that simultaneously evaluates  $u_{sh}$  and  $\Pi$ , by measuring the fully-developed velocity profile under steady flow for an applied  $E_0$  potential (which should be kept low, as in the SAOSEO, to guarantee that we are in the linear regime, i.e.  $u_{sh} \propto E_0$ ). In such condition, the steady-state velocity profile is given as:

$$u^{ss} = u_{sh} \frac{(1 + \Pi) + \bar{y}(1 - \Pi)}{2} \quad (58)$$

By fitting the linear velocity profile along  $\bar{y}$ , we can easily determine  $u_{sh}$  and  $\Pi$ . Experimentally, if no PIV or PTV system is available, a simple long exposure photography technique can be used, and by recording the length of the particle path lines at each  $\bar{y}$  position, and knowing the exposure time allows the calculation of the velocity profile.

Subsequently, for the same value of  $E_0$ , applying a sinusoidal potential difference,  $E_x = E_0 \sin(\omega t)$  allows to determine easily the factor  $\sqrt{\bar{A}^2 + \bar{B}^2}$  (which has similarities with the complex modulus amplitude in SAOS, defined as  $|G^*| = \sqrt{G'^2 + G''^2}$ ) by using the same long time exposure technique. For each  $\omega$ , the exposure time should be equal or larger than a full period of oscillation ( $\delta t \geq T = 2\pi/\omega$ ), and by measuring the length of the path lines at each position  $\Delta x_{max}$  allows to determine  $\sqrt{\bar{A}^2 + \bar{B}^2}$  since:

$$\Delta x_{max} = \left[ u_{sh} \frac{(1 + \Pi) + \bar{y}(1 - \Pi)}{2} \right] \frac{2}{\omega \sqrt{\bar{A}^2 + \bar{B}^2}} \quad (59)$$

and the function in square brackets was previously determined.

To obtain further information using the SAOSEO technique proposed requires the use of a PIV or PTV system synchronized with the voltage wave generator. By measuring the time evolution of the velocity profile along the wave cycle, allows a fit to Eq. (54) to determine the phase difference angle  $\phi$  and the parameter  $\sqrt{\bar{A}^2 + \bar{B}^2}$  (if not yet determined). Knowing these quantities,  $\bar{A}$  and  $\bar{B}$  can be easily computed since (e.g. Eq. (55)):

$$\frac{\bar{A}}{\sqrt{\bar{A}^2 + \bar{B}^2}} = \cos(\phi), \quad \frac{\bar{B}}{\sqrt{\bar{A}^2 + \bar{B}^2}} = \sin(\phi) \quad (60)$$

Now, recalling the definitions of  $\bar{A}$  and  $\bar{B}$ , we can easily compute the storage and loss moduli:

$$G' = \sum_{n=1}^m \frac{\eta_n \lambda_n \omega^2}{1 + (\lambda_n \omega)^2} = \omega B = \eta_0 \omega \bar{B}, \quad G'' = \sum_{n=1}^m \frac{\eta_n \omega}{1 + (\lambda_n \omega)^2} = \omega A = \eta_0 \omega \bar{A} \quad (61)$$

where the total shear viscosity can be easily measured at very low shear rates using a capillary viscometer.

With the proposed technique, we can easily determine the variation of  $G'$  and  $G''$  with  $\omega$ , as is usually done in SAOS, and by fitting a multi-mode model determine  $\eta_n$  and  $\lambda_n$  parameters. However, this procedure requires the fluid to remain homogeneous throughout the microchannel, i.e., such effects as polymer wall depletion or adsorption must not be present. In the presence of wall depletion, the fluid response will tend to approach that of a purely-viscous fluid, whereas wall adsorption enhances elastic effects. The experimental assessment of these effects is beyond the scope of this work, but the practical implementation of the technique calls for their minimization and such endeavor requires future research, testing different types of viscoelastic fluids and different channel wall treatments in order to assess their influence on the possible formation of wall-depletion and wall-adsorption layers. Note that it is possible to account for some of these wall effects as was done in the very elaborate general analytical solution of Sousa et al. [45] for steady flow, and by Jian et al. [46] for transient EOF of generalized Maxwell fluids, here taking into account the depletion layer effects and the Maxwell electrical stress at the interface. For other investigations on wall effects associated with polymers, the reader is referred to [47–50].

Note also that in the use of an experimental technique that relies on following/tracking a suspended particle, its motion is both due to electro-osmosis and electrophoresis and due account of the latter is required for accurate measurements as is well shown in Tatsumi et al. [51]. In particular, if the zeta potentials for the particles and micro-channel walls have the same sign, the electro-osmosis and electrophoretic velocities will have opposite signs for the same applied electric fields, which can reduce, and even cancel, the particle motion. However, if both materials have zeta potentials of opposite sign the particle velocities will be amplified. The time response of the particles will not be affected, because the characteristic response time of electrophoresis is very small. For a typical channel of 100  $\mu\text{m}$  width and suspended particles of 1  $\mu\text{m}$  diameter, time-scales of electro-osmosis (accounted for in the analytical solution) and of electrophoresis are of the order of 10 ms and 1  $\mu\text{s}$ , respectively. The experimental investigation of Sadek et al. [52] discusses these issues and existing techniques to measure the electrophoretic and electro-osmotic mobilities are reviewed.

## 5. Conclusions

Analytical solutions for the oscillatory shear flow of viscoelastic fluids driven by electro-osmotic forcing were obtained for the case of a straight microchannel with asymmetric wall zeta potentials. The rheological behavior of the fluid is described by the multi-mode upper-convected Maxwell model and the work investigates the influence of the relevant dimensionless parameters ( $\bar{\kappa}$ ,  $\omega t$ ,  $\lambda_n \omega$ ,  $Re$ ,  $M$  and  $\Pi$ ) on the normalized velocity profiles when imposing an externally potential field of the form  $E_x = E_0 \cos(\omega t)$  or  $E_x = E_0 \sin(\omega t)$ . Results for viscoelastic fluids showed that under certain operating conditions and outside the electric double layers the velocity field of the microchannel is linear and has a large amplitude of oscillation. These conditions are found at simultaneously low Reynolds number ( $Re_{cr} < 0.001$ ), thin EDL (e.g.  $\bar{\kappa}_{cr} \geq 100$ ), low Deborah number  $De$  ( $De_{cr} \leq 100$ ) and low elastic Mach number ( $M_{cr} \leq 0.32$ ). The flow linearity and magnified amplitude of these flow conditions may allow the use of this small amplitude oscillatory shear flow induced by electro-osmosis (denoted by SAOSEO) to perform rheological measurements aimed at identifying and measure the rheological characteristics of viscoelastic fluids, such as the storage ( $G'$ ) and the loss ( $G''$ ) moduli. Experimentally, in a straight microfluidic channel, measurements can be performed using a micro particle image velocimetry ( $\mu$ -PIV) system or a micro particle tracking velocimetry ( $\mu$ -PTV) system, but if neither of these systems is available, a simple long exposure photography technique can be used, but reminding that this technique is limited in terms of obtaining full measurements.

## Acknowledgments

Samir H. Sadek and Fernando Pinho acknowledge financial support from FCT (Fundação para a Ciência e a Tecnologia) through scholarship SFRH/BD/85971/2012 and project PTDC/EMS-ENE/2390/2014, respectively. Both authors acknowledge the support of CEFT (Centro de Estudos de Fenómenos de Transporte) and of funding by FCT through project UID/EMS/00532/2013 and are grateful to Prof. Manuel A. Alves for helpful discussions.

## Conflict of interest statement

The authors declare no conflict of interest.

## Supplementary material

Supplementary material associated with this article can be found, in the online version, at doi:10.1016/j.jnnfm.2019.01.007.

**Appendix A**

The  $\mathfrak{R}(\bar{u}_0)$  and the  $\mathfrak{S}(\bar{u}_0)$  constant coefficients appearing in Eq. (37) are:

$$\Phi_1 = \frac{\bar{\kappa}^2}{(\bar{A}^2 + \bar{B}^2) \{ [\cosh(2\alpha) \sin(2\sigma)]^2 + [\sinh(2\alpha) \cos(2\sigma)]^2 \} \left[ (\alpha^2 - \bar{\kappa}^2 - \sigma^2)^2 + 4\alpha^2\sigma^2 \right]} \tag{62}$$

$$\Phi_2 = (\bar{\Omega}_1 - \bar{\Omega}_2) \{ \cosh(\alpha) \sin(\sigma) [\Lambda_1 \sinh(2\alpha) \cos(2\sigma) + \Lambda_2 \cosh(2\alpha) \sin(2\sigma)] + \sinh(\alpha) \cos(\sigma) [-\Lambda_1 \cosh(2\alpha) \sin(2\sigma) + \Lambda_2 \sinh(2\alpha) \cos(2\sigma)] \} \cosh(\bar{\kappa}) \tag{63}$$

$$\Phi_3 = (\bar{\Omega}_1 - \bar{\Omega}_2) \{ \sinh(\alpha) \cos(\sigma) [-\Lambda_1 \sinh(2\alpha) \cos(2\sigma) - \Lambda_2 \cosh(2\alpha) \sin(2\sigma)] + \cosh(\alpha) \sin(\sigma) [-\Lambda_1 \cosh(2\alpha) \sin(2\sigma) + \Lambda_2 \sinh(2\alpha) \cos(2\sigma)] \} \cosh(\bar{\kappa}) \tag{64}$$

$$\Theta_1 = \frac{\bar{\kappa}^2}{2 \cosh(\bar{\kappa}) (\bar{A}^2 + \bar{B}^2) \{ [\cosh(\alpha) \cos(\sigma)]^2 + [\sinh(\alpha) \sin(\sigma)]^2 \} \left[ (\alpha^2 - \bar{\kappa}^2 - \sigma^2)^2 + 4\alpha^2\sigma^2 \right]} \tag{75}$$

$$\Phi_4 = (\bar{\Omega}_1 + \bar{\Omega}_2) \{ \sinh(\alpha) \sin(\sigma) [\Lambda_1 \sinh(2\alpha) \cos(2\sigma) + \Lambda_2 \cosh(2\alpha) \sin(2\sigma)] + \cosh(\alpha) \cos(\sigma) [-\Lambda_1 \cosh(2\alpha) \sin(2\sigma) + \Lambda_2 \sinh(2\alpha) \cos(2\sigma)] \} \sinh(\bar{\kappa}) \tag{65}$$

$$\Phi_5 = (\bar{\Omega}_1 + \bar{\Omega}_2) \{ \cosh(\alpha) \cos(\sigma) [-\Lambda_1 \sinh(2\alpha) \cos(2\sigma) - \Lambda_2 \cosh(2\alpha) \sin(2\sigma)] + \sinh(\alpha) \sin(\sigma) [-\Lambda_1 \cosh(2\alpha) \sin(2\sigma) + \Lambda_2 \sinh(2\alpha) \cos(2\sigma)] \} \sinh(\bar{\kappa}) \tag{66}$$

$$\Phi_6 = \{ [\cosh(2\alpha) \sin(2\sigma)]^2 + [\sinh(2\alpha) \cos(2\sigma)]^2 \} [\bar{A}(\alpha^2 - \bar{\kappa}^2 - \sigma^2) + 2 \bar{B} \alpha \sigma] \tag{67}$$

$$\Phi_7 = (\bar{\Omega}_1 - \bar{\Omega}_2) \{ \sinh(\alpha) \cos(\sigma) [-\Lambda_1 \sinh(2\alpha) \cos(2\sigma) - \Lambda_2 \cosh(2\alpha) \sin(2\sigma)] + \cosh(\alpha) \sin(\sigma) [-\Lambda_1 \cosh(2\alpha) \sin(2\sigma) + \Lambda_2 \sinh(2\alpha) \cos(2\sigma)] \} \cosh(\bar{\kappa}) \tag{68}$$

$$\Xi_1 = \frac{\bar{\kappa}^2}{2(\bar{A}^2 + \bar{B}^2) \{ [\sinh(2\alpha) \cos(2\sigma)]^2 + [\cosh(2\alpha) \sin(2\sigma)]^2 \} \left[ (\alpha^2 - \bar{\kappa}^2 - \sigma^2)^2 + 4\alpha^2\sigma^2 \right]} \tag{82}$$

$$\Phi_8 = (\bar{\Omega}_1 - \bar{\Omega}_2) \{ \cosh(\alpha) \sin(\sigma) [-\Lambda_1 \sinh(2\alpha) \cos(2\sigma) - \Lambda_2 \cosh(2\alpha) \sin(2\sigma)] + \sinh(\alpha) \cos(\sigma) [\Lambda_1 \cosh(2\alpha) \sin(2\sigma) - \Lambda_2 \sinh(2\alpha) \cos(2\sigma)] \} \cosh(\bar{\kappa}) \tag{69}$$

$$\Phi_9 = (\bar{\Omega}_1 + \bar{\Omega}_2) \{ \cosh(\alpha) \cos(\sigma) [-\Lambda_1 \sinh(2\alpha) \cos(2\sigma) - \Lambda_2 \cosh(2\alpha) \sin(2\sigma)] + \sinh(\alpha) \sin(\sigma) [-\Lambda_1 \cosh(2\alpha) \sin(2\sigma) + \Lambda_2 \sinh(2\alpha) \cos(2\sigma)] \} \sinh(\bar{\kappa}) \tag{70}$$

$$\Phi_{10} = (\bar{\Omega}_1 + \bar{\Omega}_2) \{ \cosh(\alpha) \cos(\sigma) [\Lambda_1 \cosh(2\alpha) \sin(2\sigma) - \Lambda_2 \sinh(2\alpha) \cos(2\sigma)] + \sinh(\alpha) \sin(\sigma) [-\Lambda_1 \sinh(2\alpha) \cos(2\sigma) - \Lambda_2 \cosh(2\alpha) \sin(2\sigma)] \} \sinh(\bar{\kappa}) \tag{71}$$

$$\Phi_{11} = \{ [\cosh(2\alpha) \sin(2\sigma)]^2 + [\sinh(2\alpha) \cos(2\sigma)]^2 \} [\bar{B}(\alpha^2 - \bar{\kappa}^2 - \sigma^2) - 2 \bar{A} \alpha \sigma] \tag{72}$$

$$\Lambda_1 = 2 \bar{A} (\alpha^2 - \bar{\kappa}^2 - \sigma^2) + 4 \bar{B} \alpha \sigma \tag{73}$$

$$\Lambda_2 = 2 \bar{B} (\alpha^2 - \bar{\kappa}^2 - \sigma^2) - 4 \bar{A} \alpha \sigma \tag{74}$$

**Appendix B**

The  $\mathfrak{R}(\bar{u}_{0 \text{ EZP}})$  and the  $\mathfrak{S}(\bar{u}_{0 \text{ EZP}})$  constant coefficients appearing in Eq. (40) are:

$$\Theta_2 = [-\Lambda_1 \cosh(\alpha) \cos(\sigma) - \Lambda_2 \sinh(\alpha) \sin(\sigma)] \cosh(\bar{\kappa}) \tag{76}$$

$$\Theta_3 = [-\Lambda_1 \sinh(\alpha) \sin(\sigma) + \Lambda_2 \cosh(\alpha) \cos(\sigma)] \cosh(\bar{\kappa}) \tag{77}$$

$$\Theta_4 = \Lambda_1 \{ [\cosh(\alpha) \cos(\sigma)]^2 + [\sinh(\alpha) \sin(\sigma)]^2 \} \tag{78}$$

$$\Theta_5 = [\Lambda_1 \sinh(\alpha) \sin(\sigma) - \Lambda_2 \cosh(\alpha) \cos(\sigma)] \cosh(\bar{\kappa}) \tag{79}$$

$$\Theta_6 = [-\Lambda_1 \cosh(\alpha) \cos(\sigma) - \Lambda_2 \sinh(\alpha) \sin(\sigma)] \cosh(\bar{\kappa}) \tag{80}$$

$$\Theta_7 = \Lambda_2 \{ [\cosh(\alpha) \cos(\sigma)]^2 + [\sinh(\alpha) \sin(\sigma)]^2 \} \tag{81}$$

**Appendix C**

The  $\mathfrak{R}(\bar{u}_{0 \text{ NZP}})$  and the  $\mathfrak{S}(\bar{u}_{0 \text{ NZP}})$  constant coefficients appearing in Eq. (43) are:

$$\Xi_2 = \sinh(\alpha) \sin(\sigma) [\Lambda_1 \sinh(2\alpha) \cos(2\sigma) + \Lambda_2 \cosh(2\alpha) \sin(2\sigma)] + \cosh(\alpha) \cos(\sigma) [-\Lambda_1 \cosh(2\alpha) \sin(2\sigma) + \Lambda_2 \sinh(2\alpha) \cos(2\sigma)] \tag{83}$$

$$\Xi_3 = \cosh(\alpha) \cos(\sigma) [-\Lambda_1 \sinh(2\alpha) \cos(2\sigma) - \Lambda_2 \cosh(2\alpha) \sin(2\sigma)] + \sinh(\alpha) \sin(\sigma) [-\Lambda_1 \cosh(2\alpha) \sin(2\sigma) + \Lambda_2 \sinh(2\alpha) \cos(2\sigma)] \tag{84}$$

$$\Xi_4 = \cosh(2\alpha) \sin(2\sigma) [-\Lambda_1 \sinh(\alpha) \cos(\sigma) + \Lambda_2 \cosh(\alpha) \sin(\sigma)] + \sinh(2\alpha) \cos(2\sigma) [\Lambda_1 \cosh(\alpha) \sin(\sigma) + \Lambda_2 \sinh(\alpha) \cos(\sigma)] \tag{85}$$

$$\Xi_5 = \sinh(2\alpha) \cos(2\sigma) [-\Lambda_1 \sinh(\alpha) \cos(\sigma) + \Lambda_2 \cosh(\alpha) \sin(\sigma)] + \cosh(2\alpha) \sin(2\sigma) [-\Lambda_1 \cosh(\alpha) \sin(\sigma) - \Lambda_2 \sinh(\alpha) \cos(\sigma)] \tag{86}$$

$$\Xi_6 = \Lambda_1 \{ [\sinh(2\alpha) \cos(2\sigma)]^2 + [\cosh(2\alpha) \sin(2\sigma)]^2 \} / \sinh(2\bar{\kappa}) \tag{87}$$

$$\Xi_7 = \cosh(\alpha) \cos(\sigma) \left[ -\Lambda_1 \sinh(2\alpha) \cos(2\sigma) - \Lambda_2 \cosh(2\alpha) \sin(2\sigma) \right] + \sinh(\alpha) \sin(\sigma) \left[ -\Lambda_1 \cosh(2\alpha) \sin(2\sigma) + \Lambda_2 \sinh(2\alpha) \cos(2\sigma) \right] \quad (88)$$

$$\Xi_8 = \cosh(\alpha) \cos(\sigma) \left[ \Lambda_1 \cosh(2\alpha) \sin(2\sigma) - \Lambda_2 \sinh(2\alpha) \cos(2\sigma) \right] + \sinh(\alpha) \sin(\sigma) \left[ -\Lambda_1 \sinh(2\alpha) \cos(2\sigma) - \Lambda_2 \cosh(2\alpha) \sin(2\sigma) \right] \quad (89)$$

$$\Xi_9 = \cosh(2\alpha) \sin(2\sigma) \cosh(\alpha) \sin(\sigma) \left[ -\Lambda_1 - \Lambda_2 \sinh(\alpha) \cos(\sigma) \right] + \sinh(2\alpha) \cos(2\sigma) \left[ -\Lambda_1 \sinh(\alpha) \cos(\sigma) + \Lambda_2 \cosh(\alpha) \sin(\sigma) \right] \quad (90)$$

$$\Xi_{10} = \cosh(2\alpha) \sin(2\sigma) \left[ \Lambda_1 \sinh(\alpha) \cos(\sigma) - \Lambda_2 \cosh(\alpha) \sin(\sigma) \right] + \sinh(2\alpha) \cos(2\sigma) \left[ -\Lambda_1 \cosh(\alpha) \sin(\sigma) - \Lambda_2 \sinh(\alpha) \cos(\sigma) \right] \quad (91)$$

$$\Xi_{11} = \Lambda_2 \left\{ [\sinh(2\alpha) \cos(2\sigma)]^2 + [\cosh(2\alpha) \sin(2\sigma)]^2 \right\} / \sinh(2\kappa) \quad (92)$$

## References

- [1] C. Zhao, E. Zholkovskij, J.H. Masliyah, C. Yang, Analysis of electroosmotic flow of power-law fluids in a slit microchannel, *J. Colloid. Interface Sci.* 326 (2) (2008) 503–510.
- [2] C. Zhao, C. Yang, Nonlinear Smoluchowski velocity for electroosmosis of power-law fluids over a surface with arbitrary zeta potentials, *Electrophoresis* 31 (5) (2010) 973–979.
- [3] C.L. Zhao, C. Yang, An exact solution for electroosmosis of non-Newtonian fluids in microchannels, *J. Non-Newtonian Fluid Mech.* 166 (17–18) (2011) 1076–1079.
- [4] F.F. Reuss, Sur un nouvel effet de l'électricité galvanique, *Mémoires de la Société Impériale des Naturalistes de Moscou* 2 (1809) 327–337.
- [5] G. Karniadakis, A. Beskok, N. Aluru, *Microflows and Nanoflows: Fundamentals and Simulation*, Springer Science Business Media Inc., USA, 2005.
- [6] P. Tabeling, *Introduction to Microfluidics*, Oxford University Press Inc., New York, 2005.
- [7] H. Bruus, *Theoretical Microfluidics*, Oxford University Press Inc., New York, 2008.
- [8] X. Wang, S. Wang, B. Gendhar, C. Cheng, C.K. Byun, G. Li, M. Zhao, S. Liu, Electroosmotic pumps for microflow analysis, *Trends Analyt. Chem.* 28 (1) (2009) 64–74.
- [9] M.S.N. Oliveira, M.A. Alves, F.T. Pinho, Microfluidic flows of viscoelastic fluids, in: R. Grigoriev (Ed.), *Transport and Mixing in Laminar Flows: From Microfluidics to Oceanic Currents*, Wiley-VCH Verlag & Co. KGaA, Weinheim, Germany, 2011.
- [10] R.G. Larson, *Constitutive Equations for Polymer Melts and Solutions: Butterworths Series in Chemical Engineering*, Butterworth-Heinemann, Boston, 1988.
- [11] R.B. Bird, R.C. Armstrong, O. Hassager, *Dynamics of polymeric liquids, Vol. 1: Fluid Mechanics*, A Wiley-Interscience Publication, John Wiley & Sons, New York, 1987.
- [12] G.B. Thurston, Rheological parameters for the viscosity, viscoelasticity and thixotropy of blood, *Biorheology* 16 (3) (1979) 149–162.
- [13] M. Renardy, Existence of slow steady flows of viscoelastic fluids with differential constitutive equations, *ZAMM J. Appl. Math. Mech. / Zeitschrift für Angewandte Mathematik und Mechanik* 65 (9) (1985) 449–451.
- [14] M. Renardy, Are viscoelastic flows under control or out of control? *Syst. Control Lett.* 54 (12) (2005) 1183–1193.
- [15] E. Savelev, M. Renardy, Control of homogeneous shear flow of multimode Maxwell fluids, *J. Non-Newtonian Fluid Mech.* 165 (3–4) (2010) 136–142.
- [16] D. Rajagopalan, R.C. Armstrong, R.A. Brown, Calculation of steady viscoelastic flow using a multimode Maxwell model: Application of the explicitly elliptic momentum equation (EEME) formulation, *Journal of Non-Newtonian Fluid Mechanics* 36 (1990) 135–157.
- [17] P.A. Vasquez, M.G. Forest, Complex fluids and soft structures in the human body, in: S.E. Spagnolie (Ed.) *Complex Fluids in Biological Systems*, Springer, New York, 2015, pp. 53–110.
- [18] S.S. Thete, P. Doshi, H.V. Pol, New insights into the use of multi-mode phenomenological constitutive equations to model extrusion film casting process, *J. Plastic Film Sheeting* 33 (1) (2017) 35–71.
- [19] M. Zinet, R. El Otmani, M.H. Boutaous, P. Chantrenne, Numerical modeling of non-isothermal polymer crystallization kinetics: Flow and thermal effects, *Polym. Eng. Sci.* 50 (10) (2010) 2044–2059.
- [20] S.A. Prost-Domasky, B. Khomami, A note on start-up and large amplitude oscillatory shear flow of multimode viscoelastic fluids, *Rheologica Acta* 35 (3) (1996) 211–224.
- [21] Z. Liu, L.E. Bilston, Large deformation shear properties of liver tissue, *Biorheology* 39 (6) (2002) 735–742.
- [22] M. Hrapko, J. van Dommelen, G. Peters, J. Wismans, Large strain behaviour of brain tissue in shear and compression, *J. Biomech.* 39 (2006) S154–S155.
- [23] S. Das, S. Chakraborty, Analytical solutions for velocity, temperature and concentration distribution in electroosmotic microchannel flows of a non-Newtonian bio-fluid, *Analytica Chimica Acta* 559 (1) (2006) 15–24.
- [24] S. Chakraborty, Electroosmotically driven capillary transport of typical non-Newtonian biofluids in rectangular microchannels, *Anal. Chim. Acta* 605 (2) (2007) 175–184.
- [25] C. Zhao, C. Yang, Analysis of power-law fluid flow in a microchannel with electrokinetic effects, *Int. J. Emerg. Multi. Fluid Sci.* 1 (1) (2009) 37–52.
- [26] H.M. Park, W.M. Lee, Helmholtz-Smoluchowski velocity for viscoelastic electroosmotic flows, *J. Colloid Interface Sci.* 317 (2) (2008) 631–636.
- [27] H.M. Park, W.M. Lee, Effect of viscoelasticity on the flow pattern and the volumetric flow rate in electroosmotic flows through a microchannel, *Lab Chip* 8 (7) (2008) 1163–1170.
- [28] A.M. Afonso, M.A. Alves, F.T. Pinho, Analytical solution of mixed electro-osmotic/pressure driven flows of viscoelastic fluids in microchannels, *J. Non-Newtonian Fluid Mech.* 159 (1–3) (2009) 50–63.
- [29] A.M. Afonso, M.A. Alves, F.T. Pinho, Electro-osmotic flow of viscoelastic fluids in microchannels under asymmetric zeta potentials, *J. Eng. Math.* 71 (1) (2011) 15–30.
- [30] S. Dhinakaran, A.M. Afonso, M.A. Alves, F.T. Pinho, Steady viscoelastic flow between parallel plates under electro-osmotic forces: Phan-Thien-Tanner model, *J. Colloid Interface Sci.* 344 (2) (2010) 513–520.
- [31] H. Morgan, N.G. Green, *AC electrokinetics: Colloids and Nanoparticles*, Research Studies Press Ltd, UK, 2003.
- [32] S. Chakraborty, *Microfluidics and Microfabrication*, Springer, London, 2010.
- [33] P. Dutta, A. Beskok, Analytical solution of time periodic electroosmotic flows: analogies to Stokes' second problem, *Anal. Chem.* 73 (21) (2001) 5097–5102.
- [34] S. Chakraborty, A.K. Srivastava, Generalized model for time periodic electroosmotic flows with overlapping electrical double layers, *Langmuir* 23 (24) (2007) 12421–12428.
- [35] Q.S. Liu, Y.J. Jian, L.G. Yang, Time periodic electroosmotic flow of the generalized Maxwell fluids between two micro-parallel plates, *J. Non-Newtonian Fluid Mech.* 166 (9–10) (2011) 478–486.
- [36] A.C. Bogaerds, W.M. Verbeeten, G.W. Peters, F.P. Baaijens, 3D viscoelastic analysis of a polymer solution in a complex flow, *Comput. Methods Appl. Mech. Eng.* 180 (3–4) (1999) 413–430.
- [37] R.B. Bird, W.E. Stewart, E.N. Lightfoot, *Transport Phenomena*, John Wiley & Sons, Inc., New York, 2002.
- [38] A.M. Afonso, F.T. Pinho, M.A. Alves, Electro-osmosis of viscoelastic fluids and prediction of electro-elastic flow instabilities in a cross slot using a finite-volume method, *J. Non-Newtonian Fluid Mech.* 179–180 (2012) 55–68.
- [39] J.H. Masliyah, S. Bhattacharjee, *Electrokinetic and colloid transport phenomena*, Wiley-Interscience, Hoboken, New Jersey, 2006.
- [40] P. Dutta, A. Beskok, Analytical solution of combined electroosmotic/pressure driven flows in two-dimensional straight channels: Finite Debye layer effects, *Anal. Chem.* 73 (9) (2001) 1979–1986.
- [41] D. Burgreen, F.R. Nakache, Electrokinetic flow in ultrafine capillary slits, *J. Phys. Chem.* 68 (5) (1964) 1084–1091.
- [42] M.S. Kilic, M.Z. Bazant, A. Ajdari, Steric effects in the dynamics of electrolytes at large applied voltages. I. Double-layer charging, *Phys. Rev. E* 75 (2) (2007) 021502.
- [43] D.O.A. Cruz, F.T. Pinho, Fully-developed pipe and planar flows of multimode viscoelastic fluids, *J. Non-Newtonian Fluid Mech.* 141 (2–3) (2007) 85–98.
- [44] D.O.A. Cruz, F.T. Pinho, Stokes' second problem with wall suction or blowing for UCM fluids, *J. Non-Newtonian Fluid Mech.* 157 (1–2) (2009) 66–78.
- [45] J.J. Sousa, A.M. Afonso, F.T. Pinho, M.A. Alves, Effect of the skimming layer on electro-osmotic-Poiseuille flows of viscoelastic fluids, *Microfluid. Nanofluid.* 10 (1) (2011) 107–122.
- [46] Y. Jian, J. Su, L. Chang, Q. Liu, G. He, Transient electroosmotic flow of general Maxwell fluids through a slit microchannel, *Zeitschrift für angewandte Mathematik und Physik* 65 (3) (2013) 435–447.
- [47] F.-M. Chang, H.-K. Tsao, Drag reduction in electro-osmosis of polymer solutions, *Appl. Phys. Lett.* 90 (19) (2007) 194105.
- [48] M.L. Olivares, L. Vera-Candioti, C.L. Berli, The EOF of polymer solutions, *Electrophoresis* 30 (5) (2009) 921–929.
- [49] O.A. Hickey, J.L. Harden, G.W. Slater, Molecular dynamics simulations of optimal dynamic uncharged polymer coatings for quenching electro-osmotic flow, *Phys. Rev. Lett.* 102 (10) (2009) 108304.
- [50] C.L. Berli, The apparent hydrodynamic slip of polymer solutions and its implications in electrokinetics, *Electrophoresis* 34 (5) (2013) 622–630.
- [51] K. Tatsumi, K. Nishitani, K. Fukuda, Y. Katsumoto, K. Nakabe, Measurement of electroosmotic flow velocity and electric field in microchannels by micro-particle image velocimetry, *Measure. Sci. Technol.* 21 (10) (2010) 105402.
- [52] S.H. Sadek, F. Pimenta, F.T. Pinho, M.A. Alves, Measurement of electroosmotic and electrophoretic velocities using pulsed and sinusoidal electric fields, *Electrophoresis* 38 (7) (2017) 1022–1037.